Measurement Report: Spatial and vertical variability of aerosol optical properties during MOABAI mobile on-road campaign in North China Plain

Ioana E. Popovici[1,2], Zhaoze Deng[3], Philippe Goloub[1], Xiangao Xia[3], Hongbin Chen[3], Luc Blarel[1], Thierry Podvin[1], Yitian Hao[3,a], Hongyan Chen[3], Disong Fu[3], Nan Yin[3], Benjamin Torres[1], Stéphane Victori[2], Xuehua Fan[3]

[1] Univ. Lille, CNRS, UMR8518 – LOA – Laboratoire d'Optique Atmosphérique, 59000 Lille, France

[2] R&D Department, Cimel Electronique, Paris, 75011, France

[3] LAGEO, Institute of Atmospheric Physics, Chinese Academy of Sciences, Beijing, 100029, China

[a] now at: Meteorological Centre of Southwest Air Traffic Management Bureau, CAAC (Civil Aviation Administration of China), Chengdu, 610200, China

Correspondence to: Ioana E. Popovici (i-popovici@cimel.fr)

Abstract. The North China Plain (NCP) has been experiencing serious air quality problems since the rapid urbanization and industrialization and has been the subject of many studies over the years. This work presents mapping at a fine scale of the aerosol spatial and vertical variability obtained during the MOABAI campaign (Mobile Observation of Atmosphere By vehicle-borne Aerosol measurement Instruments) using a van equipped with a micro-pulse LIDAR, a sun photometer and in situ instruments, performing on-road measurements. The campaign was conducted from 5 May to 23 May 2017 and had as a main objective to map the pollutants distribution in Beijing and NCP area. A summary of aerosol properties during all measurement days and a comprehensive case study along the industrial Binhai New Area near Tianjin are presented. The highest AOD at 440 nm (1.34 and 1.9) were recorded during two heavy pollution episodes on 18 May and 19 May 2017, respectively. The lowest PBL (Planetary Boundary Layer) heights (< 1500 m) were recorded during the heavy pollution events, correlated with the highest AOD. Transport of dust from Gobi Desert was captured during the mobile measurements,

25   impacting Beijing in the 9-13 May period. Exploring the NCP outside Beijing provided datasets in regions with lack of

aerosol observation sites and allowed mapping higher aerosol concentrations when passing by polluted cities in NCP

(Baoding, Tianjin and Tangshan). In this study, we provide the first mass concentration profiles derived from a mobile

micro-pulse LIDAR, making use of complementary information on aerosol type from sun photometer and in situ data. The

case study of 17 May 2017 revealed mean extinction coefficients of 0.14 ± 0.10 km^{-1} at 532 nm and total mass concentration

30   of 80 ± 62 µg m^{-3} in the PBL (< 2000 m) for the mobile transect from Tianjin to Tangshan along the coast of Bohai Sea. The

highest extinction (0.56 km^{-1}) and mass concentrations (404 µg m^{-3}) were found in the industrial Binhai New Area. The PM$_{10}$

and PM$_{2.5}$ fractions of the total mass concentration profiles were separated using the columnar size distribution derived from

sun photometer measurements. A general good agreement was found between the lidar-derived PM concentrations at surface

level and the ones recorded at the closest air quality stations along the transect, with the only exception along the industrial

35   region near Tianjin port, where emissions were highly variable.

1 Introduction

The North China Plain (NCP) in north-eastern China is one of the most populated and polluted regions of China, where long-

standing heavy aerosol pollution episodes frequently occur (Chen and Wang, 2015; Yang et al., 2018). The region has

undergone rapid development of urbanization and industrialization for rapid economic growth leading to a deterioration in

40   air quality (Han et al., 2015) and becoming one of the regions with the most severe air pollution in China. Some of the most

polluted cities in China (Beijing, Baoding, Tianjin, Tangshan, Shijiazhuang) are here and air pollution has become an

important concern in this region (An et al., 2019; Sun et al., 2017; Zhu et al., 2016). The major contributor to air pollution is

particulate matter (PM), mainly fine particulate matter (PM$_{2.5}$) emitted from fossil fuel, biomass burning, and urban

construction (Lei et al., 2011). The NCP is also impacted by frequent dust storms in spring (Yu et al., 2017), studies showing

45   an increase in dust presence in northeast and northwest regions (Li, 2020). Regional transport plays an important role in

urban air pollution. Both local and regional sources contribute to the air pollution in the NCP region, depending on the

synoptic conditions, desert dust being advected over NCP when air flows are dominated by westerly winds (Sun et al., 2001)

while fine particles pollution events occur with southern winds flow (Chen and Wang, 2015). The measures taken through

air pollution control policies show an improvement of air quality and a negative trend for $PM_{2.5}$ concentrations since 2013

50   (Ma et al., 2018; Zhai et al., 2019). Nonetheless, the pollution levels are still high in NCP, especially during haze episodes,

and exceed the air quality limits locally. The ambient air quality standards of the World Health Organization (WHO) for 24 h

average are 25 µg m^{-3} for $PM_{2.5}$ and 50 µg m^{-3} for PM_{10}, lower than those established by the Ministry of Ecology and

Environment of the People's Republic of China (MEE), of 35-75 µg m^{-3} for $PM_{2.5}$ and 50-150 µg m^{-3} for PM_{10}. The diversity

of emissions and the mixture of pollutants result in complex physical, chemical and optical properties of aerosols in the NCP

55   region, making it an interesting area to study. A number of investigations of air pollution in the NCP achieved using

observation sites, aircrafts measurements, mobile laboratories, satellite data and air quality models have been conducted over

the years. A review of these studies in NCP is given in Zhu et al. (2016). The observation sites in NCP are generally located

in or around large cities, mostly around Beijing, and cannot capture the spatial variability of pollutants at a fine scale. In

order to address the air pollution problems in the NCP, it is necessary to identify the distribution of air pollutants in the

60   region and their transport. Observations from a limited number of measurement sites cannot describe this spatial variability

and the transport of pollutants in the NCP. For this, a mobile instrumented laboratory performing on-road measurements is

useful for identifying the sources of pollution and the areas exceeding the air pollution limits and the regional transport of

aerosols.

In this paper, we report on-road remote sensing and in situ measurements of the optical properties, particle size distributions,

65   and spatial and vertical distribution of aerosols in Beijing and NCP area in the 9-19 May 2017 period conducted with a

3

mobile instrumented vehicle. The optical properties of aerosols at surface level were measured by in situ. The total column volume size distribution was derived from spectral aerosol optical depth (AOD) measurements. The extinction coefficient profiles derived from LIDAR measurements were converted into total mass concentration profiles with a mass extinction efficiency (MEE) approach. These properties are reported for different pollution levels and for a case study along Tianjin

70   port.

2 MOABAI campaign

The MOABAI campaign (Mobile Observation of Atmosphere By vehicle-borne Aerosol measurement Instruments) has been carried out from 5 to 23 May 2017 in North China Plain. The transects of the mobile measurements and the IAP (Institute of Atmospheric Physics) mobile platform are shown in Fig. 1. Remote sensing and in situ instrumentation were involved in the

75   campaign in order to map the spatial and vertical variability of key aerosol properties in Beijing and other polluted cities in the NCP (Baoding, Tianjin, Tangshan). Mobile measurements have been conducted on 10 days, out of which 6 days in Beijing on the 4th, 5th and 6th ring-roads by day and by night and 4 days outside of Beijing, on the Beijing–Baoding–Tianjin, Tianjin – Tangshan, Tangshan - Beijing and Beijing - Xiahuayuan transects, as shown in Fig.1b.

2.1 Mobile laboratory

80   The on-road mobile measurements were conducted with the IAP mobile laboratory shown in Fig.1c, a Mercedes Benz 416 CDI diesel van (length 6.72 m, width 2.01 m, height 2.89 m; payload 5.6 tons). A power generator operated by the engine could continuously supply power when the van was on. An uninterrupted power supply was employed to regulate the voltage and frequency of electricity and could support all instruments for around 8 h when engine was not working. A cooling system inside the van was used to maintain the temperature constant. The van was equipped with aerosol remote sensing and

85   in situ instruments as well as real-time monitoring trace gas analysers. Table 1 gives an overview of all the instruments on

board the mobile laboratory, the measured parameters and the temporal resolution and uncertainty for each measurement. Only the measurements of aerosol properties by remote sensing and in situ instruments will be presented in this study. Gas-phase parameters measured are not discussed in this study.

The CE370 CIMEL micro-pulse LIDAR (lidar) and the PLASMA (Photomètre Léger Aéroporté pour la Surveillance des

90   Masses d'Air) sun photometer from MAMS (Mobile Aerosol Monitoring System) payload (Popovici et al., 2018) were transported and integrated on site in the existing IAP van already equipped with in situ instruments and gas analysers. The lidar and the sun photometer have been previously used for on-road mobile measurements in France and have been described in details (Popovici et al., 2018). The lidar provided vertical profiles of aerosols and clouds in the troposphere, from 200 m up to around 12000 m altitude (molecular detection range, dependent on aerosol concentration) with a vertical resolution of

95   15 m. The data quality was assured by following the Rayleigh fit protocol defined by EARLINET (Freudenthaler et al., 2018). The comparison of the lidar profiles to the molecular profile computed for air density represents the absolute calibration of lidar signals and allows access further to the geophysical parameters such as the backscatter/extinction profiles. The uncertainties of the lidar profiles and the derived parameters have been previously discussed (Popovici et al., 2018) and are shown in Table 1.

100   PLASMA is the only mobile sun photometer able to track the sun during the vehicle's motion, meets the AERONET standards and is included in the network, referenced as instrument #650. Compared to CIMEL CE318 sun photometers in AERONET, the current PLASMA model performs only direct sun measurements. The instrument is calibrated by Service National d'Observation, SNO PHOTONS/AERONET-EARLINET, component of ACTRIS (Aerosols, Clouds and Trace gases Research InfraStructure) and French component of AERONET. PLASMA follows the AERONET calibration protocol

105   for the reference master instrument and is also intercalibrated regularly against a master sun photometer from PHOTONS

network at Observatoire de Haute Provence (OHP) in France before and after a field campaign. This allows checking the stability of the instrument over time as its characteristics may change.

The in situ instruments consisted of a polar 3-λ nephelometer (Aurora 4000 model, Ecotech) (Müller et al., 2011), a 7-λ aethalometer (AE33, Maggee Scientific) (Drinovec et al., 2015), a Sky-OPC (11S, GRIMM Aerosol Technik) and trace gas

110   analysers for NO_2, SO_2 and O_3. Aerosol was sampled using an isokinetic inlet facing forward. The sampled air was split into two flows. One flow was open and directly exposed to in-car air in order to remove the excess air and reduce the pressure in instrument inlets. Tests showed that van speed higher than 20 km h^{-1} could ensure that the open flow was large enough to prevent in-car air to be sampled by instruments downstream. The other flow passed through a nafion drier (MD-700, Perma Pure) and then entered the nephelometer and aethalometer. The Sky-OPC had a separate isokinetic inlet, which could adapt

115   the air velocity within a range of 16-25 m s^{-1} (the speed of van was approximately 60-90 km h^{-1} when assuming the wind speed was 0) using a nozzle with the opening of 1 mm. The gas analysers were calibrated using standard gases before the campaign. The nephelometer was calibrated using air and R134 before the campaign. The flow of the aethalometer was checked before and after the campaign.

Finally, the van was equipped with a weather station that measured the meteorological data (ambient pressure, temperature,

120   relative humidity and wind speed/direction). The driving speed was kept around 90 km h^{-1} (25 m s^{-1}), in order to cover as much distance as possible in the NCP region. For the in situ aerosol and gas measurements, the position of the inlets at 3.3 m above the ground, at the front of the van, was intended to reduce self-pollution from the van's exhaust. The driving speed was also maintained constant when possible, in order to provide a constant sampling flow rate and to reduce contamination from the van's exhaust. The driving speed was higher than the normal wind speed, thereby during the measurements the

125   particles from the exhaust could not reach the inlet in front of the vehicle as a result of the wind from the back of the vehicle.

Atmospheric
Chemistry
and Physics
Discussions

Open Access

EGU

The effects of self-pollution can be neglected for the remote sensing instruments as they measure either columnar parameters or vertical profiles starting from 200 m above ground level.

2.2 Methods

A Klett-Fernald-based (Fernald, 1984; Klett, 1981) backward inversion algorithm called BASIC (Mortier, 2013; Mortier et

130   al., 2013a) was used to invert the lidar data in synergy with the sun photometer data. The algorithm requires the lidar range corrected signals (RCS) and the measured AOD to constrain the inversion. The products derived are: extinction coefficient profiles, height-independent lidar ratios (LR) resulted from the iterative process and cloud, aerosol layers and PBL heights. The algorithm's description and applications to real data have been previously shown (Mortier et al., 2013a, 2016; Popovici, 2018; Popovici et al., 2018). The sources of uncertainties have been described (Popovici et al., 2018) and the overall

135   uncertainty for the retrieved aerosol extinction coefficient profiles is considered to be 25%.

In situ measurements were also used in lidar inversion, to improve the extinction profile in the lidar blind zone (0-200 m). The scattering and absorption coefficients measured by the nephelometer and the aethalometer, respectively, were used to compute the extinction coefficients at surface level and a linear interpolation was applied between the lidar-derived extinction value at 200 m and the extinction measured by in situ at surface level.

140   Nonetheless, care needs to be taken with in situ instruments as they measure the properties of dry particles and not in ambient conditions as it is done by lidar. Some aerosols can uptake water and the effect of relative humidity (RH) is rather constant up to 70%, but a sharp increase of scattering and extinction coefficients is shown for RH>70% (Randriamiarisoa et al., 2006; Skupin et al., 2016). The scattering coefficients measured by the nephelometer were corrected for the RH effect following Eq. (1) (Pan et al., 2009):

145    $$\sigma_{sca,wet} = f(RH)\sigma_{sca,dry} \tag{1}$$

where $\sigma_{sca,dry}$ is the dry scattering coefficient measured by the nephelometer and $f(RH)$ is the aerosol hygroscopic growth factor, defined by the empirical equation Eq. (2) (Pan et al., 2009):

$$f(RH) = 1 + a\,(RH/100)^b \tag{2}$$

where a and b are fitting parameters for specific aerosol types, found in literature. The values used for the case study will be

150   discussed in the dedicated section. For measurements when the RH > 40% a correction has been applied, using the RH measured by the weather station on the roof of the mobile platform. The aerosol absorption coefficients were obtained from aethalometer measurements, using correction factors obtained in a comparison study in Beijing between the aethalometer and a 3-wavelength Photoacoustic Soot Spectrometer (PASS-3, Droplet Measurement Technologies).

We used GRASP (Dubovik et al., 2011, 2014, 2019) algorithm and software (https://www.grasp-open.com/, last access: 24

155   March 2020) to retrieve the columnar aerosol volume size distribution (VSD) from spectral AOD measurements performed on-road with PLASMA sun photometer. The GRASP application for only direct sun measurements, called GRASP-AOD, has been previously described (Torres et al., 2017). It relies on statistically optimized fitting of the sun photometer observations and the aerosol is assumed as a mixture of spherical and non-spherical particles, with a defined sphere fraction and an assumed refractive index for the dominant aerosol type. The retrievals provide the six parameters describing the

160   lognormal size distributions for the fine and coarse mode. The uncertainties of the retrieved size distributions lie within 5-10% for the fine mode and within 10-20% for the coarse mode (Torres et al., 2017). In this study we show the GRASP-AOD retrievals for a case study of mobile on-road measurements along Tianjin port.

A Mass Extinction Efficiency (MEE) approach (Lagrosas et al., 2005; Lewandowski et al., 2010) has been used to convert the aerosol extinction coefficient profiles derived from the lidar-sun-photometer-in-situ synergy into mass concentration

165   profiles. The MEE relates the total column extinction coefficient to the total mass concentration of aerosols, computed for defined aerosol characteristics, and is defined by Eq. (3) (Lewandowski et al., 2010):

$$MEE = \frac{\pi \int_{r_{min}}^{r_{max}} r^2 Q_{ext}(r,m,\lambda) n(r) dr}{\frac{4}{3}\pi\rho \int_{r_{min}}^{r_{max}} r^3 n(r) dr} \quad \left[\frac{1/m}{g/m^3}\right] \tag{3}$$

where r is the particle size, r_{min} and r_{max} are the limits of the particles size distribution, $n(r)$ is the number size distribution,

Q_{ext} is the Mie extinction efficiency computed for 532 nm, m is the assumed refractive index and ρ is the particle density.

170   The MEE has been computed assuming spherical particles and the following aerosol properties: columnar volume size

distribution (VSD) retrieved with GRASP-AOD, assumed refractive index and characteristic particle density for fine and

coarse modes. The aerosol mass concentration profiles, $M(z)$, have been derived using Eq. (4):

$$M(z) = \frac{\sigma_{ext}(z)}{MEE} \quad \left[\frac{\mu g}{m^3}\right] \tag{4}$$

where $\sigma_{ext}(z)$ is the aerosol extinction coefficient profile and MEE has been previously defined.

175   This methodology has been previously applied for volcanic ash mass concentration estimations (Mortier et al., 2013) and for

mass concentrations profiles for mobile observations in France (Popovici et al., 2018). The uncertainty on the mass

concentration profiles comes from the uncertainties on the extinction coefficient profiles, the aerosol size distribution, the

assumed refractive index and the particles density. The overall uncertainty on the mass concentration profiles is estimated to

be between 35% and 45%. The parameters used for computing the MEE and their uncertainty for the case study are

180   presented in the results section.

3 Results

3.1 Overview of aerosol properties

An overview of the aerosol optical properties is presented in this section, namely the AOD and Angstrom Exponent (AE)

from PLASMA sun photometer and the Range Corrected Signals (RCS) and Planetary Boundary Layer (PBL) height from

185   lidar on-road measurements in NCP.

Atmospheric
Chemistry
and Physics
Discussions

3.1.1 Spatial distribution of AOD and Angstrom Exponent

The spatial distribution of AOD at 440 nm and Angstrom Exponent (AE) between 440 and 870 nm are shown in Fig. 2. The maps show the aerosol optical properties variability at different scales: fine scale (5x3 km grid) of the city of Beijing (Fig. 2a and Fig. 2g), medium scale (50x30 km grid) around the 5th ring road of Beijing (Fig. 2b-c and Fig. 2h-i) and regional scale

190 (200x250 km grid) in the Great Plain of North China (Fig. 2e and Fig. 2k). A different AOD scale was chosen for each figure in order to show the fine spatial variability. The details of each mobile transect, the AOD, AE and PBL height ranges are summarized in Table 2. Four mobile observations (9, 11, 13 and 19 May) were conducted on Beijing's 4th, 5th and 6th ring-roads (Fig. 2a-d, Fig. 2f and Fig. 2g-j, Fig. 2l) and three of the mobile observations were carried out outside Beijing, in the NCP, on 16 May (Beijing– Baoding-Tianjin (AB)), 17 May (Tianjin-Tangshan (BC)) and 18 May (Tangshan-Beijing (CA))

195 (Fig. 2e and Fig. 2k). Five types of days were observed: one day of heavy pollution (0.72 ± 0.06) in Beijing (9 May) with desert dust contribution (AE of 0.79 ± 0.05), one dust episode (AE of 0.05 ± 0.07) in Beijing (11 May) with moderate aerosol loading (0.37 ± 0.07), one clean day (0.12 ± 0.02) in Beijing (13 May) but still with dust contribution (AE of 0.67 ± 0.04), two moderate pollution days (0.32-0.45) outside Beijing (16 and 17 May) consisting mainly of fine particles (AE of 1.12-1.23), but also with desert dust contribution in altitude and two heavy pollution (0.86-1.69) days (18 and 19 May), with

200 predominance of fine particles (AE of 1.31-1.41). Low AE values were recorded when north-westerly winds prevailed, Beijing and NCP being downwind of Asian dust storms, on the transport path from Gobi desert, while the highest AOD and AE were recorded during regional heavy pollution episodes when air masses moved from the south. For the moderate pollution and clean situations there was a contribution of both fine and coarse particles, indicated by AE values between those for dust and fine particles episodes. For indication, the average AOD and AE in Beijing during spring are 0.8 and 1,

205 respectively (Yu et al., 2017). Lower AE in spring compared to other seasons show the impact of dust episodes, as observed also during our mobile measurements in MOABAI campaign.

3.1.2 Vertical variability and PBL height

Figure 3 shows the vertical distribution of aerosol layers and clouds as seen by the mobile lidar during the on-road

measurements in NCP. Most days were clear sky, except for 16 and 19 May afternoon, when cirrus clouds were present,

210 explaining the lack of AOD measurements. The AOD at 440 nm and the PBL height are also depicted in Fig. 3 to show the

correlation between the low PBL height and the high AOD values.

HYSPLIT (Hybrid Single Particle Lagrangian Integrated Trajectory, Stein et al., 2015) backward trajectories for 72 h were

performed for all days. For 9 May, which was a pollution day with dust intrusion, the air masses originated from S direction

for the layers up to 2000 m above ground level, while the aerosol layers at 3000-4000 m altitude were transported from NW

215 direction, suggesting desert dust component (also suggested by lower AE values). The back trajectories for the dust episode

(11 May) showed air masses from NW direction (Inner Mongolia), transporting dust from Gobi desert. For the clean day (13

May) air masses originated from N, bringing clean air over Beijing, with a small contribution of residual dust up to 4000 m

altitude. The dust event in the 11-14 May 2017 period has been discussed in Li et al. (2018). Higher particle concentrations

near the surface (increase in lidar backscatter signal) and lower PBL height compared to previous days were observed when

220 passing by polluted cities (Baoding, Tianjin, Tangshan) and industrial regions (Tianjin coastal area). The lowest PBL height

(500-1700 m) were recorded on the days with moderate and heavy fine particles pollution (16, 17, 18 and 19 May), when air

masses flowed from S and SW directions, passing over polluted cities in the NCP (Baoding, Shijiazhuang, Tianjin). The

lofted aerosol layers observed at around 2000 m above ground level on 16 May and around 3000 m altitude on 17 May

originate from N and NW directions, suggesting dust contribution. For the heavy pollution days (18 and 19 May) there is a

225 clear correlation between the high AOD (0.86-1.69) and the low PBL height (500-1600 m). It has been previously reported

that heavy pollution episodes occur when the air masses move from S direction (Yu et al., 2017). Our mobile measurements

showed also that heavy pollution episodes impact the whole NCP region.

Atmospheric
Chemistry
and Physics
Discussions
EGU
Open Access

3.2 Case study: Tianjin coastal area, 17 May 2017

3.2.1 Study area and meteorological conditions

230   The mobile transect and the local time of measurements are presented in Fig. 4a. We started the mobile measurements at

08:30 local time (UTC+08:00) from the city of Tianjin, heading south and then continuing along the Bohai sea coast, passing

through the industrialized Binhai New Area in the 12:00 - 13:30 time interval and then heading northeast to Tangshan and

stopping at Guye around 16:00 local time. The weather was fair, with clear sky along the whole transect, ambient

temperatures (T) in the 24°-30° C range and relative humidity (RH) in the 30-65 % range, with a noticeable increase of RH

235   along the coast (Fig. 5c). Backward trajectories (Fig. 8b) at 0 m and 500 m altitude show a S-SE flux and a NW direction for

the air masses at 3000 m. It has been reported that southerly winds are associated with heavy pollution (Chen and Wang,

2015; He et al., 2009; Yu et al., 2017), while advection of desert dust to an elevation of < 3000 m is common when air flows

are dominated by westerly winds (Sun et al., 2001).

The Binhai New Area, about 60 km east of Tianjin city, is an important economic coastal area with large industrial activities,

240   including Tianjin port, the largest port in Northern China and one of the largest ports in the world. The industry sectors vary

from machinery factories, petro-chemical manufacturing plants, automotive fitting factories and electronics facilities to sea

salt production, shipbuilding and port activity and logistics. The area accounted 271 industrial enterprises in 2012, resulting

in heavy pollution in the region (Kong et al., 2010; Su et al., 2017). Both natural and anthropogenic sources such as wind

and soil erosion, sea salt, fossil-fuel combustion, vehicles emissions, construction activities, industrial processes and

245   photochemical reactions contribute to the Particulate Matter (PM), resulting in a complex chemical composition of particles

in this region (Ni et al., 2013). It is an interesting study area where the microphysical and optical properties of aerosols are

not well characterized, much less at a fine scale. The situation is even more complex in spring as mineral dust transports

occur frequently, adding to the anthropogenic pollution. One previous study showing mobile lidar measurements has been

conducted in Tianjin, in different seasons of 2016 (Lyu et al., 2018). Another study by Su et al. (2017) presents the

250 variability of aerosol microphysical and optical properties as measured by sun photometers set up at three sites, urban,

industrial and coastal areas of Tianjin. Nevertheless, this is the first time on-road mobile lidar, sun photometer and in situ

measurements are conducted in Tianjin coastal area.

3.2.2 Particle size distribution at surface level

Mean volume size distributions measured by Sky-OPC on 30 minutes road segments are presented in Fig. 4b. In the fine

255 mode, three peaks are observed, centered at 0.28, 0.45 and 0.65 μm diameter. In the supermicron range, a broad coarse mode

is observed between 1 and 5 μm, with a distinct peak at 3.5 μm, seen all along the mobile transect, and a coarse mode

centered at 7.5 μm. Super-coarse particles (> 10 μm) with mode diameters centered at 13, 18 and 30 μm are most probably

re-suspended dust. The highest concentrations are observed at 0.28 μm, showing that fine particles pollution is

predominating at surface level. The sampled aerosol were a mixture of regional scale background aerosol and direct emission

260 of vehicles and industry. Both soot and secondary aerosol could contribute significantly in the submicron ambient aerosol.

Hildemann et al. (1991) showed that the mass size distributions of both gasoline and diesel cars emissions present a single

mode with a peak at 0.2 μm. Studies on ship emissions show that particles with $D_p < 0.3$ μm dominate (Merico et al., 2016;

Petzold et al., 2008), which could also explain the increase of the fine mode centered at 0.28 μm when passing by the Tianjin

port in our case. The peak at 0.65 μm could correspond to particulate sulphate and ammonium, as shown by Zhuang et al.

265 (1999) in a study conducted on a coastal site in Hong Kong. According to the same study, the nitrates dominated at a coarse

mode diameter of 3.95 μm, which could explain the peak at 3.5 μm in our case. The explanation for the high increase in

particle concentrations in the Binhai New Area is two-fold. On one hand, we passed by a region with significant higher

pollution (industry emissions, intense traffic emissions), so higher particles concentrations. On the other hand, the increase in

concentration could be an effect of particle growth in the presence of higher RH. A clear correlation between the increase of

270   RH and the increase of particles concentrations is seen in Fig. 5. It has been shown that ship exhaust particles are highly

hygroscopic in humid marine environment (Popovicheva et al., 2009). In our case, if particles smaller than 0.25 μm (the

minimum detectable diameter of Sky-OPC) would increase in size due to water uptake, they would be counted in the upper

size bins, resulting in an increase of particles number in the upper size bins. An increase in concentration is observed for

particles in the $0.25 < D_p < 0.8$ μm range, meaning that, according to our hypotheses, these particles could be more

275   hygroscopic and affected by water uptake. Another interesting event depicted in Fig. 5 is a clear episode of sea breeze,

between 12:10 and 13:40, marked by sudden increase of RH correlated with drop in temperature. This sea breeze event

suggests that sea salt was transported inland. Sea salt have diameters higher than 0.3 μm and are highly hygroscopic

(Randles et al., 2004). According to the review of Heintzenberg et al. (2000), the size distribution of marine aerosols presents

3 distinct modes in the fine mode, centered at 0.05, 0.15 and 0.4 μm diameter, which could explain the increase of particles

280   at 0.45 but this does not suffice to discriminate a marine aerosol contribution.

3.2.3 Aerosol scattering and absorption at surface level

The scattering (at 525 nm), absorption (at 520 nm) and extinction coefficients derived from nephelometer and aethalometer

measurements at surface level, as well as the T and RH monitored by the mobile weather station are presented in Fig. 5. The

aethalometer data was averaged on 30 s and the RH correction to scattering coefficients (Eq. (1) in Sect. 2.2) was applied to

285   the nephelometer data in order to compute the ambient (wet) extinction coefficients at surface level. The a and b parameters

in Eq. (2) used for the RH correction are as follows: i) $a = 2.3$ and $b = 6.27$ for the polluted aerosol type according to Pan

et al. (2009) on the pollution segments of the mobile transect (08:40-12:00 and 13:30-16:00 local time) and ii) $a = 3.26$ and

$b = 3.27$, following Liu et al. (2008) for mixed urban-marine aerosols for the transects with sea salt intrusion (12:00-13:30

local time). The mean absorption, scattering (wet) and extinction at surface level were 0.05 ± 0.03 km^{-1}, 0.24 ± 0.11 km^{-1} and

290   0.29 ± 0.12 km^{-1} respectively, where the standard deviations represent the spatio-temporal variability along the route. An

Atmospheric
Chemistry
and Physics
Discussions
Open Access
EGU

increase of both scattering and absorption coefficients is observed in the 12:00-13:30 time interval, when scattering rises as high as 0.83 km^{-1} and absorption up to 0.22 km^{-1}. The mean SSA (Single Scattering Albedo) for the whole transect was 0.84 ± 0.07.

Figure 6 shows the comparison between the in situ extinction coefficients at surface level and the lidar-derived extinction at

295   210 m altitude (retrieved using a constant extrapolation in the inversion). Both dry and ambient (wet) extinction coefficients from in situ data are depicted in order to show the impact of the $f(RH)$ correction on the segments where the RH > 50%. The lidar-derived extinction coefficients at 210 m altitude agree very well with the in situ extinction at surface level. This good agreement between lidar and in situ gives confidence in the overlap correction used for the lidar data and shows that the assumption of homogeneity from the surface up to ~200 m altitude (constant extrapolation) is reasonable for most of the

300   mobile measurements. Significant differences are observed in the 12:00-13:30 time interval, probably due to the inhomogeneity of the aerosol distribution from ground to 200 m altitude. The extinction in this time interval measured by in situ and corrected for RH effects, is on average 2 times higher than the lidar-derived extinction. The differences could be explained by the strong increase in particle concentration and/or change in aerosol type only at the surface level and not be « seen » at 200 m altitude by the lidar. Secondly, the aerosol mixture assumption and the $f(RH)$ correction applied to the

305   nephelometer data could be not appropriate, resulting in an overestimation of scattering coefficients. The lidar-derived extinction coefficients at surface level are highly correlated with the extinction measured by in situ with R^2 of 0.98, slope of 0.91 and RMSE of 0.03 all along the transect excluding the values in the 12:00 – 13:30 time interval. The correlation decreases when including the values in this time interval (R^2 of 0.9, slope of 0.53, RMSE of 0.08).

3.2.4 Columnar volume size distribution

310   The total column aerosols volume size distributions (VSD) retrieved with GRASP-AOD from PLASMA sun photometer measurements are presented in Fig. 7c-d. Spectral AOD (Fig. 7b) and AE (Fig. 7a) from PLASMA measurements averaged

on 30 minutes transects, as in Fig. 4a, are also presented. The inversion requires the assumption of the refractive index and of

the sphere fraction. Assumptions on the aerosols chemical composition were made based on the modes identified in the in-

situ-derived size distributions at surface level. An important contribution of elemental carbon (EC), organic carbon (OC) and

315   sulphates was considered, indicated by the narrow fine mode peak at 0.28 μm, followed by a nitrates component, suggested

by the coarse mode centered at 3.5 μm, a small contribution of dust in altitude (from lidar data and backward trajectories

analysis) and sea salt contribution during the sea breeze event. According to a study conducted in Tianjin, in spring 2009

(Han et al., 2012), an average refractive index of 1.52-0.018i was found for a similar aerosol mixture as in our case. For the

retrievals, the assumption of spherical particles and a complex refractive index of 1.52-0.008i were used for most of the

320   transect. A lower absorption (imaginary part) was considered taking into account that desert dust was present in the free

troposphere. For the part along the coast (12:00-13:30) a complex refractive index of 1.46-0.008i was used, considering the

RH effect on aerosols and the sea breeze event, following the results from Schuster et al. (2009) for the aerosol types in our

case (fine particles that are predominantly sulphates) and for the maximum relative humidity (60 – 65%). The columnar size

distributions present two modes, fine and coarse, centered at 0.3 μm and 3.4 μm diameter, respectively. The size distributions

325   do not change significantly over the mobile transect, except for an increase in both fine and coarse modes concentrations

when reaching the polluted coastal region. The increase in fine mode can be explained by higher particle number

concentrations as discussed in Sect. 3.2.2 and the increase in coarse mode along the coast could be explained by the sea salt

intrusion during the sea breeze and increase of the nitrates component. The change in particle size is shown by both AE (Fig.

7a) and VSD (Fig. 7c). The highest AE values and slightly higher fine mode were observed in Tianjin, followed by a

330   decrease in AE and an increase of coarse mode in the VSD between 10:00 and 11:30. In the coastal industrial region, the

concentrations of both fine and coarse modes increase significantly and AE increases but is still lower than at Tianjin due to

an important contribution of coarse mode. The columnar aerosol fine mode concentrations increase by two times in the

Atmospheric
Chemistry
and Physics
Discussions

12:00-13:30 time interval, consistent with what is seen at the surface level. Both in situ and columnar VSD present the same

positions of the fine and coarse modes diameter at 0.3 and 3.5 μm, respectively, which shows that the two major aerosol

335   contributions in the fine mode were sulphates and black carbon (BC) and nitrates in the coarse mode.

3.2.5 Extinction coefficient profiles

The spatial variability of the extinction coefficients profiles at 532 nm derived from the synergy of lidar and sun photometer

measurements is represented in Fig. 8a. The lidar Klett inversion constrained by AOD was used to get the extinction profiles

and the in situ constraint between surface and 200 m altitude. The mean extinction coefficient in the PBL, from the surface

340   to about 2000 m, was 0.14 ± 0.10 km^{-1} along the whole transect from Tianjin to Tangshan and extinction reaching a

maximum of 0.56 km^{-1} when passing by the industrial coastal region. Table 3 presents the summary of the derived variables,

the mean extinction coefficients, lidar ratios and mass concentrations up to 2000 m altitude for each transect in Fig. 4a. The

standard deviations depict the spatio-temporal variability for each segment. The highest extinction coefficients were found

near Tianjin city and along the industrial Binhai New Area along the coast of Bohai Sea. Some examples of extinction

345   coefficient and mass concentration profiles along the route are depicted in Fig. 9: at Tianjin (08:55), between Tianjin and

Binhai New Area (10:50), when crossing a salt pan (12:30), when crossing Tianjin port (13:00) and near Tangshan (15:20).

In the free troposphere, an elevated aerosol layer at 2200–3500 m was observed all along the mobile transect. The HYSPLIT

backward trajectories at 0 m, 500 m and 3000 m, starting at 13:00 local time (05:00 UTC), illustrated in Fig. 8b, show that

the layer at about 3000 m is transported from Inner Mongolia while the aerosols in the PBL have a local origin. The

350   separation of the elevated dust layer (Fig. 10) has been done using the first derivative of the extinction profiles and applying

a threshold to separate the aerosol contributions above PBL. The mean extinction coefficient of the dust layer was $0.05 \pm$

0.03 km^{-1}, with a maximum of 0.15 km^{-1} at 2900 m around 10:30. The mean AOD at 532 nm of the dust layer is 0.06 ± 0.01,

which represents 18-20% of the total measured AOD.

The variability of height-independent extinction-to-backscatter ratio or lidar ratios (LR) at 532 nm derived from lidar-sun-

355 photometer inversions is presented in Table 3 for each segment of the mobile transect. The standard deviations correspond to

the spatio-temporal variability in each segment. The LR values decrease from 66 ± 10 sr at Tianjin to 35 ± 12 sr when

crossing the Binhai New Area and then increase again to 57 ± 14 sr near Tangshan. The decrease in the LR indicates a

change in the aerosol type. The LR around 60 sr, found at Tianjin and Tangshan, are characteristics for urban-industrial

aerosol type (Cattrall et al., 2005; Müller et al., 2007) while the LR around 40 sr correspond to a marine aerosol type

360 (Ackermann, 1998; Müller et al., 2001, 2007). In our case it is most probably a mixture of continental polluted and marine

polluted aerosols (considering the sources along the coast), with a contribution of desert dust in altitude. The values found at

Tianjin and Tangshan are consistent with a study in Shangdianzi, located in the northern part of the North China Plain, where

a mean LR of 60 sr was found (Hänel et al., 2012). The LR found along the coast are similar to the values of 33 ± 14 sr

found at a site on the French coast (Boyouk et al., 2011) and of 40 sr found on the Portuguese coast (Ansmann et al., 2001).

365 Both studies evidenced the presence of a sharp peak in the backscatter signal in the marine boundary layer ranging between

200 and 650 m when the air masses were coming from the sea direction, which is similar to what is observed in our case, a

strong increase in the scattering coefficients below 200 m when reaching the coast. The sea salt presence in the atmosphere

in this region is evident as salt pans are located at the places where the peaks were observed. The Tianjin municipality has a

long history of sea salt exploitation and there were still two saltpans exploited at that time according to (Wang et al., 2015),

370 illustrating the coastal landscape map of Tianjin Binhai New Area in 2013. The strong increase of extinction coefficients

seen below 200 m and decrease of the columnar LR correspond to the time intervals when the mobile system was crossing

the salt pans and could be linked to a strong presence of sea salt.

3.2.6 Mass concentration profiles

The vertical profiles of aerosols total mass concentration derived from lidar measurements using the Mass Extinction

375 Efficiency (MEE) approach described in Sect. 2.2 are presented in Fig. 10. For this method we used complementary

information on the aerosol volume size distributions (VSD), particle density (ρ) and complex refractive index (CRI). The

mean columnar VSD derived from sun photometer measurements showed an almost equal contribution of fine and coarse

mode particles all along the mobile transect. For the estimations of the mass concentration, the parameters of the mean VSD

were used (Table 4). Using the aerosol properties previously discussed, we defined an urban-industrial aerosol model for the

380 particles inside the PBL, up to 2000 m, and a desert dust model for the dust layer at 2200-3500 m. The parameters for the

urban-industrial aerosol model are summarized in Table 4. As shown is Sect. 3.2.5, the dust layer in the free troposphere was

found to be around 20% of the total AOD, so from the total column coarse particles. This contribution was subtracted from

the total coarse VSD and the rest of the VSD was considered as characteristic for the aerosols in the PBL (< 2000 m). A bi-

modal VSD and a ratio of coarse-to-fine mode particles concentration (Cc/Cf) of 0.8 was used for the mass calculations for

385 the PBL. The average particle density was calculated based on the chemical composition (sulphate, nitrate, EC, OC, residue)

and correspondent particle densities (1.76, 1.73, 2, 1.4, 2.3 g cm^{-3}) following Han et al. (2012), and using the sea salt density

(1.3 g cm^{-3}) as in Tsekeri et al. (2017). A value of 1.75 g cm^{-3} was obtained for particles inside the PBL. The CRI used for

the mass calculations was 1.52-0.008i. For the dust aerosol model, we used a mono-modal coarse mode VSD, a CRI of 1.5 −

0.005i and a particle density of 2.6 g cm^{-3}, characteristic for desert dust. The standard deviations of the parameters in Table 4

390 correspond to the variability of the retrieved VSD presented in Fig. 7d and were propagated to the calculations, to show the

impact of different parameters on the mass concentrations estimations (Table 4). An MEE of 1.79 m^2 g^{-1} was found for the

fine-dominant aerosol model in the PBL and an MEE of 0.54 m^2 g^{-1} for the dust layer. Other studies found MEE values of

0.5-1.09 m^2 g^{-1} for Saharan dust (Córdoba-Jabonero et al., 2016). For fine particles, a higher MEE (2.87-6.64 m^2 g^{-1}) was

found for PM$_{2.5}$ in cities in China (Cheng et al., 2017), but in our case the size distribution shows an important contribution

395   of both coarse and fine particles.

Some examples of mass concentration profiles are presented in Fig. 9. The mean mass concentration in the dust layer was 95

± 52 µg m^{-3} with a maximum of 284 µg m^{-3}. The mean total mass concentration in the PBL, for different segments along the

mobile transect, is presented in Table 4 and is around 80 ± 62 µg m^{-3} for the whole transect. The standard deviations

represent the variability along each transect segment. The highest particle mass concentrations were recorded near Tianjin

400   city, until 09:30, and when crossing the industrial coastal region, from 12:00 to 14:00. The PM$_{10}$ and PM$_{2.5}$ fractions of the

total particle mass concentrations were calculated as the percentage of particles with D$_p$ < 10 µm and D$_p$ < 2.5 µm,

respectively, from the total volume concentration of the VSD defined for aerosols in the PBL. Using this method, it was

found that the PM$_{10}$ and PM$_{2.5}$ represented 95 % and 56 %, respectively, of the total mass. The lidar-derived PM$_{10}$ and PM$_{2.5}$

mass concentrations at surface level and the hourly PM$_{10}$ and PM$_{2.5}$ recorded at air quality (AQ) stations along the mobile

405   transect are presented in Fig. 11. The PM$_{10}$ and PM$_{2.5}$ measured at the AQ stations closest to the mobile transect were

considered. Despite all the limits for a direct comparison with AQ measurements and the uncertainties and assumptions used

for the calculations, there is a rather good agreement between the lidar-derived mass and AQ measurements.

The estimation of aerosol mass concentration is a complex issue involving numerous assumptions, namely the particles size

distribution, particles shape, chemical composition, mixing state and the homogeneity and stationarity of all these parameters

410   with height. Thus, the associated uncertainties are also difficult to be evaluated. In this study, the standard deviation of each

parameter given in Table 4 was used as a measure of the uncertainty. To this adds the uncertainty on the extinction profiles,

considered to be 25%. The highest uncertainty is introduced by the assumed particle density, with an impact of 20 %,

followed by the complex refractive index, with an impact of 13 % on the mass concentration. Considering the errors as

statistically independent, an overall uncertainty of 32 % was evaluated for mass concentration profiles. The levels recorded

415 at AQ are within the uncertainty of the estimated mass concentrations. In order to give an order of magnitude for the

difference between the air quality and the lidar-derived mass concentrations, a mean difference was calculated considering

the hourly means from AQ stations and the closest value in time from lidar data. A mean difference of 10 % and 42 % was

obtained for PM_{10} and $PM_{2.5}$, respectively. This comparison is only indicative, since the hourly mean concentrations

recorded at air quality stations are not directly comparable with the 1-minute mass concentrations from mobile

420 measurements. Despite all the assumptions and uncertainties involved in the mass concentration calculations, we believe that

the advantages of this method for lidar community and for aerosol data modelling outweigh its limitations.

4 Conclusions

Numerous studies on air pollution have already been performed in North China Plain region, although, there are none

conducting measurements during motion with mobile lidar and mobile sun photometer. The novelty of this study consists in

425 observations with a mobile vehicle equipped with lidar, sun photometer and in situ instruments (nephelometer, aethalometer,

particle counter) deployed to capture the aerosols spatial distribution in Beijing and NCP. Constraining the lidar inversion

with a lidar ratio (LR) computed using the AOD measured by the sun photometer is closer to reality than inversion with a

pre-defined constant LR for all profiles, that might not be relevant for the aerosol spatial variability observed along a mobile

transect. Most lidars do not see well close to the surface, and therefore miss important part of the boundary layer.

430 Photometers measure all the atmospheric column, including this layer never seen by lidar or not accurately seen by lidar. In

situ data at surface level complement the missing information from lidar. The combination lidar-photometer-in-situ is the

only way to profile properly the entire aerosol column, which is presented in this study. In addition, there is a European

effort made in the frame of ACTRIS (Aerosol Cloud and Trace Gas infrastructure) research infrastructure, to put these three

distinct communities (lidar, photometer and in situ) working together since synergies are the solution for future and open the

435 way to many new applications. For example, this method is applicable to fixed sites having in situ, lidar and sun photometer.

The applications of such mobile system having lidar and sun photometer are numerous. Mapping AOD with a mobile sun

photometer allows the validation of satellite measurements at different scales; no other instrument at ground can do that

spatially in so many points. Studies showing profiles of aerosol mass concentration are scarce in the literature. The new

scientific results presented in this study are profiles of aerosols mass concentration (not only at surface level) computed

440 using an improved method (lidar, sun photometer and in situ), that allows more accurate calculations, compared to other

methods. Different aerosol plumes (smoke, dust, volcanic) and their variability can be tracked spatially to the source and

their contribution (AOD, mass concentration) to the vertical profile evaluated. We showed the added value of such mobile

system through the MOABAI campaign.

A summary of the various atmospheric situations (clean, pollution, dust) observed during MOABAI campaign and of the

445 AOD, Angstrom Exponent and PBL height was given. A comprehensive analysis focused on a case study in a heavily

polluted and complex area, between Tianjin and Tangshan cities and the Tianjin port (Binhai New Area) was presented.

Profiles of aerosols mass concentration were derived from lidar-sun-photometer-in-situ synergy. Using the columnar volume

size distribution retrieved from AOD sun photometer measurements, we evaluated the PM_{10} and $PM_{2.5}$ fractions of the total

mass concentrations at ground level, which compare well to the air quality measurements. The results presented show the

450 potential capabilities of lidar measurements for air quality applications, such as mapping spatially the PM_{10} and $PM_{2.5}$

concentrations at surface level and vertically using a mobile system. Mass concentration profiles of dust, volcanic ash and

smoke plumes and their spatial distribution are key parameters for different authorities. These measurements are valuable for

aviation alerts in case of disruptive events (such as volcanic ash intrusions) and tracking aerosols dynamics and regional

Atmospheric
Chemistry
and Physics
Discussions

transport, useful for air quality modelling. The results of this work demonstrate that a mobile instrumented vehicle is an

455 excellent tool for the real-time characterization of aerosol variability and of pollution levels both spatially and vertically.

As perspective to improve the mass concentration profiles, depolarization and spectral lidar measurements will be used to

better characterize the aerosol types on the vertical profile. This will be achieved with the dual-wavelength, depolarization

micro-lidar CIMEL CE376, which was deployed for mobile on-road measurements of smoke in FIREX-AQ (Fire Influence

on Regional to Global Environments and Air Quality) campaign in northwestern US in summer 2019, and for stationary

460 measurements during COBIACC (Campagne d'Observation Intensive des Aérosols et précurseurs à Caillouël-Crépigny)

campaign in France (also in summer 2019), focused on monitoring of background and transported aerosols at a rural site.

The mobility of sun photometers is advancing also. On one side, the Cimel CE318-T sun-sky-lunar photometer has already

been involved successfully in shipborne campaigns (Yin et al., 2019) and was also deployed during FIREX-AQ for mobile

car measurements. On the other side, the development of an Advanced PLASMA instrument, performing sun and sky

465 measurements, is in progress. Recently, in France, Marion Dufresne ship in operation in the Indian Ocean has been equipped

with such Cimel CE318-T mobile photometer to measure on a permanent basis what AERONET usually measures at a fixed

site. In a second step a lidar will be set up also on this mobile exploratory platform. This is opening a new era for mobile

automatic lidar and photometer joint observations, really needed to upgrade the MAN (Maritime Aerosol Network, maritime

branch of AERONET) still relying on manual measurements. These additional examples show that the number of

470 applications is increasing to which the ACTRIS European effort will contribute with the development of such lidar-

photometer retrievals.

Atmospheric
Chemistry
and Physics
Discussions

Author contributions. The project was conceived and supervised by HC, XX, XF and PG. IP, LB, HC, YH and ZD

participated to the field campaign. IP and ZD performed the data analysis. BT helped with GRASP-AOD inversions. IP

480   wrote the manuscript of this paper and all the co-authors contributed with corrections.

24

Atmospheric
Chemistry
and Physics
Discussions

500

References

Ackermann, J.: The extinction-to-backscatter ratio of tropospheric aerosol: A numerical study, J. Atmos. Ocean. Technol.,

15(4), 1043–1050, doi:10.1175/1520-0426(1998)015<1043:TETBRO>2.0.CO;2, 1998.

An, Z., Huang, R. J., Zhang, R., Tie, X., Li, G., Cao, J., Zhou, W., Shi, Z., Han, Y., Gu, Z. and Ji, Y.: Severe haze in

505   northern China: A synergy of anthropogenic emissions and atmospheric processes, Proc. Natl. Acad. Sci. U. S. A., 116(18),

8657–8666, doi:10.1073/pnas.1900125116, 2019.

Ansmann, A., Wagner, F., Althausen, D., Müller, D., Herber, A. and Wandinger, U.: European pollution outbreaks during

ACE 2: Lofted aerosol plumes observed with Raman lidar at the Portuguese coast, J. Geophys. Res. Atmos., 106(D18),

20725–20733, doi:10.1029/2000JD000091, 2001.

510   Boyouk, N., Léon, J. F., Delbarre, H., Augustin, P. and Fourmentin, M.: Impact of sea breeze on vertical structure of aerosol

optical properties in Dunkerque, France, Atmos. Res., 101(4), 902–910, doi:10.1016/j.atmosres.2011.05.016, 2011.

Cattrall, C., Reagan, J., Thome, K. and Dubovik, O.: Variability of aerosol and spectral lidar and backscatter and extinction

ratios of key aerosol types derived from selected Aerosol Robotic Network locations, J. Geophys. Res. D Atmos., 110(10),

1–13, doi:10.1029/2004JD005124, 2005.

515   Chen, H. and Wang, H.: Haze days in North China and the associated atmospheric circulations based on daily visibility data from 1960 to 2012, J. Geophys. Res., 120(12), 5895–5909, doi:10.1002/2015JD023225, 2015.

Cheng, Z., Ma, X., He, Y., Jiang, J., Wang, X., Wang, Y., Sheng, L., Hu, J. and Yan, N.: Mass extinction efficiency and extinction hygroscopicity of ambient PM2.5 in urban China, Environ. Res., 156(February), 239–246, doi:10.1016/j.envres.2017.03.022, 2017.

520   Córdoba-Jabonero, C., Andrey-Andrés, J., Gómez, L., Adame, J. A., Sorribas, M., Navarro-Comas, M., Puentedura, O., Cuevas, E. and Gil-Ojeda, M.: Vertical mass impact and features of Saharan dust intrusions derived from ground-based remote sensing in synergy with airborne in-situ measurements, Atmos. Environ., 142, 420–429, doi:10.1016/j.atmosenv.2016.08.003, 2016.

Drinovec, L., Močnik, G., Zotter, P., Prévôt, A. S. H., Ruckstuhl, C., Coz, E., Rupakheti, M., Sciare, J., Müller, T.,
525   Wiedensohler, A. and Hansen, A. D. A.: The "dual-spot" Aethalometer: An improved measurement of aerosol black carbon with real-time loading compensation, Atmos. Meas. Tech., 8(5), 1965–1979, doi:10.5194/amt-8-1965-2015, 2015.

Dubovik, O., Herman, M., Holdak, A., Lapyonok, T., Tanré, D., Deuzé, J. L., Ducos, F., Sinyuk, A. and Lopatin, A.: Statistically optimized inversion algorithm for enhanced retrieval of aerosol properties from spectral multi-angle polarimetric satellite observations, Atmos. Meas. Tech., 4(5), 975–1018, doi:10.5194/amt-4-975-2011, 2011.

530   Dubovik, O., Lapyonok, T., Litvinov, P., Herman, M., Fuertes, D., Ducos, F., Torres, B., Derimian, Y., Huang, X., Lopatin, A., Chaikovsky, A., Aspetsberger, M. and Federspiel, C.: GRASP: a versatile algorithm for characterizing the atmosphere, SPIE Newsroom, 2–5, doi:10.1117/2.1201408.005558, 2014.

Dubovik, O., Li, Z., Mishchenko, M. I., Tanré, D., Karol, Y., Bojkov, B., Cairns, B., Diner, D. J., Espinosa, W. R., Goloub, P., Gu, X., Hasekamp, O., Hong, J., Hou, W., Knobelspiesse, K. D., Landgraf, J., Li, L., Litvinov, P., Liu, Y., Lopatin, A.,
535   Marbach, T., Maring, H., Martins, V., Meijer, Y., Milinevsky, G., Mukai, S., Parol, F., Qiao, Y., Remer, L., Rietjens, J.,

Sano, I., Stammes, P., Stamnes, S., Sun, X., Tabary, P., Travis, L. D., Waquet, F., Xu, F., Yan, C. and Yin, D.: Polarimetric remote sensing of atmospheric aerosols: Instruments, methodologies, results, and perspectives, J. Quant. Spectrosc. Radiat. Transf., 224, 474–511, doi:10.1016/j.jqsrt.2018.11.024, 2019.

Fernald, F. G.: Analysis of atmospheric lidar observations: some comments., Appl. Opt., 23(5), 652,

540   doi:10.1364/AO.23.000652, 1984.

Freudenthaler, V., Linné, H., Chaikovski, A., Rabus, D. and Groß, S.: EARLINET lidar quality assurance tools, Atmos. Meas. Tech. Discuss., 1–35, doi:10.5194/amt-2017-395, 2018.

Han, L., Zhou, W. and Li, W.: Increasing impact of urban fine particles (PM2.5) on areas surrounding Chinese cities, Sci. Rep., 5, 11–16, doi:10.1038/srep12467, 2015.

545   Han, S., Bian, H., Zhang, Y., Wu, J., Wang, Y., Tie, X., Li, Y., Li, X. and Yao, Q.: Effect of aerosols on visibility and radiation in spring 2009 in Tianjin, China, Aerosol Air Qual. Res., 12(2), 211–217, doi:10.4209/aaqr.2011.05.0073, 2012.

Hänel, A., Baars, H., Althausen, D., Ansmann, A., Engelmann, R. and Sun, J. Y.: One-year aerosol profiling with EUCAARI Raman lidar at Shangdianzi GAW station: Beijing plume and seasonal variations, J. Geophys. Res. Atmos., 117(13), 1–11, doi:10.1029/2012JD017577, 2012.

550   He, X., Li, C., Lau, A. K. H., Deng, Z., Mao, J., Wang, M. and Liu, X.: An intensive study of aerosol optical properties in Beijing urban area, Atmos. Chem. Phys. Discuss., 9(3), 11413–11440, doi:10.5194/acpd-9-11413-2009, 2009.

Heintzenberg1, J., Covert2, D. C. and Van Dingenen3, R.: Size distribution and chemical composition of marine aerosols: a compilation and review, Tellus, 52, 1104–1122, doi:10.1034/j.1600-0889.2000.00136.x, 2000.

Hildemann, L. M., Markowski, G. R., Jones, M. C. and Cass, G. R.: Submicrometer aerosol mass distributions of emissions

555   from boilers, fireplaces, automobiles, diesel trucks, and meat-cooking operations, Aerosol Sci. Technol., 14(1), 138–152, doi:10.1080/02776829108959478, 1991.

Klett, J. D.: Stable analytical inversion solution for processing lidar returns., Appl. Opt., 20(2), 211–220, doi:10.1364/AO.20.000211, 1981.

Kong, S., Han, B., Bai, Z., Chen, L., Shi, J. and Xu, Z.: Receptor modeling of PM2.5, PM10 and TSP in different seasons
560   and long-range transport analysis at a coastal site of Tianjin, China, Sci. Total Environ., 408(20), 4681–4694, doi:10.1016/j.scitotenv.2010.06.005, 2010.

Lagrosas, N., Kuze, H., Takeuchi, N., Fukagawa, S., Bagtasa, G., Yoshii, Y., Naito, S. and Yabuki, M.: Correlation study between suspended particulate matter and portable automated lidar data, J. Aerosol Sci., 36(4), 439–454, doi:10.1016/j.jaerosci.2004.10.007, 2005.

565   Lei, Y., Zhang, Q., He, K. B. and Streets, D. G.: Primary anthropogenic aerosol emission trends for China, 1990-2005, Atmos. Chem. Phys., 11(3), 931–954, doi:10.5194/acp-11-931-2011, 2011.

Lewandowski, P. A., Eichinger, W. E., Holder, H., Prueger, J., Wang, J. and Kleinman, L. I.: Vertical distribution of aerosols in the vicinity of Mexico City during MILAGRO-2006 Campaign, Atmos. Chem. Phys., 10(3), 1017–1030, doi:10.5194/acp-10-1017-2010, 2010.

570   Li, J.: Pollution trends in China from 2000 to 2017: A multi-sensor view from space, Remote Sens., 12(2), doi:10.3390/rs12020208, 2020.

Li, W., Wang, W., Zhou, Y., Ma, Y., Zhang, D. and Sheng, L.: Occurrence and reverse transport of severe dust storms associated with synoptic weather in East Asia, Atmosphere (Basel)., 10(1), doi:10.3390/atmos10010004, 2018.

Liu, X., Cheng, Y., Zhang, Y., Jung, J., Sugimoto, N., Chang, S. Y., Kim, Y. J., Fan, S. and Zeng, L.: Influences of relative
575   humidity and particle chemical composition on aerosol scattering properties during the 2006 PRD campaign, Atmos. Environ., 42(7), 1525–1536, doi:10.1016/j.atmosenv.2007.10.077, 2007.

Lyu, L., Dong, Y., Zhang, T., Liu, C., Liu, W., Xie, Z., Shi, Y. and Shu, X.: Vertical Distribution Characteristics of PM2.5

Observed by a Mobile Vehicle Lidar in Tianjin, China in 2016, J. Meteorol. Res., 32(February), doi:10.1007/s13351-018-7068-z.1.Introduction, 2018.

580 Ma, Z., Liu, R., Liu, Y. and Bi, J.: Effects of air pollution control policies on PM2.5 pollution improvement in China from 2005 to 2017: a satellite based perspective, Atmos. Chem. Phys. Discuss., 1–23, doi:10.5194/acp-2018-1191, 2018.

Merico, E., Donateo, A., Gambaro, A., Cesari, D., Gregoris, E., Barbaro, E., Dinoi, A., Giovanelli, G., Masieri, S. and Contini, D.: Influence of in-port ships emissions to gaseous atmospheric pollutants and to particulate matter of different sizes in a Mediterranean harbour in Italy, Atmos. Environ., 139(July), 1–10, doi:10.1016/j.atmosenv.2016.05.024, 2016.

585 Mortier, A.: Tendances et variabilites de l'aerosol atmospherique a l'aide du couplage Lidar/Photometre sur les sites de Lille et Dakar, University of Lille., 2013.

Mortier, A., Goloub, P., Podvin, T., Deroo, C., Chaikovsky, A., Ajtai, N., Blarel, L., Tanre, D. and Derimian, Y.: Detection and characterization of volcanic ash plumes over Lille during the Eyjafjallajökull eruption, Atmos. Chem. Phys., 13(7), 3705–3720, doi:10.5194/acp-13-3705-2013, 2013a.

590 Mortier, A., Goloub, P., Podvin, T., Deroo, C., Chaikovsky, A., Ajtai, N., Blarel, L., Tanre, D. and Derimian, Y.: Detection and characterization of volcanic ash plumes over Lille during the Eyjafjallajökull eruption, Atmos. Chem. Phys., 13(7), 3705–3720, doi:10.5194/acp-13-3705-2013, 2013b.

Mortier, A., Goloub, P., Derimian, Y., Tanré, D., Podvin, T., Blarel, L., Deroo, C., Marticorena, B., Diallo, A. and Ndiaye, T.: Climatology of aerosol properties and clear-sky shortwave radiative effects using lidar and sun photometer observations 595 in the Dakar site, J. Geophys. Res., 121(11), 6489–6510, doi:10.1002/2015JD024588, 2016.

Müller, D., Franke, K., Wagner, F., Althausen, D., Ansmann, A. and Heintzenberg, J.: Vertical profiling of optical and physical particle properties over the tropical Indian Ocean with six-wavelength lidar 1. Seasonal cycle, J. Geophys. Res. Atmos., 106(D22), 28567–28575, doi:10.1029/2000JD900784, 2001.

29

Müller, D., Ansmann, A., Mattis, I., Tesche, M., Wandinger, U., Althausen, D. and Pisani, G.: Aerosol-type-dependent lidar

600   ratios observed with Raman lidar, J. Geophys. Res. Atmos., 112(16), doi:10.1029/2006JD008292, 2007.

Müller, T., Laborde, M., Kassell, G. and Wiedensohler, A.: Design and performance of a three-wavelength LED-based total

scatter and backscatter integrating nephelometer, Atmos. Meas. Tech., 4(6), 1291–1303, doi:10.5194/amt-4-1291-2011,

2011.

Ni, T., Li, P., Han, B., Bai, Z., Ding, X., Wang, Q., Huo, J. and Lu, B.: Spatial and temporal variation of chemical

605   composition and mass closure of ambient pm10 in Tianjin, China, Aerosol Air Qual. Res., 13(6), 1832–1846,

doi:10.4209/aaqr.2012.10.0283, 2013.

Pan, X. L., Yan, P., Tang, J., Ma, J. Z., Wang, Z. F., Gbaguidi, A. and Sun, Y. L.: Observational study of influence of

aerosol hygroscopic growth on scattering coefficient over rural area near Beijing mega-city, Atmos. Chem. Phys., 9(19),

7519–7530, doi:10.5194/acp-9-7519-2009, 2009.

610   Petzold, A., Hasselbach, J., Lauer, P., Baumann, R., Franke, K., Gurk, C., Schlager, H. and Weingartner, E.: Experimental

studies on particle emissions from cruising ship, their characteristic properties, transformation and atmospheric lifetime in

the marine boundary layer, Atmos. Chem. Phys., 8(9), 2387–2403, doi:10.5194/acp-8-2387-2008, 2008.

Popovicheva, O., Kireeva, E., Shonija, N., Zubareva, N., Persiantseva, N., Tishkova, V., Demirdjian, B., Moldanová, J. and

Mogilnikov, V.: Ship particulate pollutants: Characterization in terms of environmental implication, J. Environ. Monit.,

615   11(11), 2077–2086, doi:10.1039/b908180a, 2009.

Popovici, I. E.: Aerosol spatial and temporal variability as seen by Mobile Aerosol Monitoring System (MAMS),

http://www.theses.fr [online] Available from: http://www.theses.fr/2018LIL1R070 (Accessed 1 October 2019), 2018.

Popovici, I. E., Goloub, P., Podvin, T., Blarel, L., Loisil, R., Unga, F., Mortier, A., Deroo, C., Victori, S., Ducos, F., Torres,

B., Delegove, C., Choël, M., Pujol-Söhne, N. and Pietras, C.: Description and applications of a mobile system performing

620   on-road aerosol remote sensing and in situ measurements, Atmos. Meas. Tech, 11, 4671–4691, doi:10.5194/amt-11-4671-

2018, 2018.

Randles, C. A., Russell, L. M. and Ramaswamy, V.: Hygroscopic and optical properties of organic sea salt aerosol and

consequences for climate forcing, Geophys. Res. Lett., 31(16), 4–7, doi:10.1029/2004GL020628, 2004.

Randriamiarisoa, H., Chazette, P., Couvert, P., Sanak, J. and Mégie, G.: Relative humidity impact on aerosol parameters in a

625   Paris suburban area, Atmos. Chem. Phys., 6(5), 1389–1407, doi:10.5194/acp-6-1389-2006, 2006.

Schuster, G. L., Lin, B. and Dubovik, O.: Remote sensing of aerosol water uptake, Geophys. Res. Lett., 36(3), 1–5,

doi:10.1029/2008GL036576, 2009.

Skupin, A., Ansmann, A., Engelmann, R., Seifert, P. and Müller, T.: Four-year long-path monitoring of ambient aerosol

extinction at a central European urban site: Dependence on relative humidity, Atmos. Chem. Phys., 16(4), 1863–1876,

630   doi:10.5194/acp-16-1863-2016, 2016.

Stein, A. F., Draxler, R. R., Rolph, G. D., Stunder, J., Cohen, M. D. and Ngan, F.: NOAA'S HYSPLIT ATMOSPHERIC

TRANSPORT AND DISPERSION MODELING SYSTEM, Bull. Am. Meteorol. Soc., 96(12), 2059–2077,

doi:10.1175/BAMS-D-14-00110.2, 2015.

Su, X., Wang, Q., Li, Z., Calvello, M., Esposito, F., Pavese, G., Lin, M., Cao, J., Zhou, C., Li, D. and Xu, H.: Regional

635   transport of anthropogenic pollution and dust aerosols in spring to Tianjin — A coastal megacity in China, Sci. Total

Environ., 584–585(April 2018), 381–392, doi:10.1016/j.scitotenv.2017.01.016, 2017.

Sun, J., Zhang, M. and Liu, T.: Spatial and temporal characteristics of dust storms in China and its surrounding regions,

1960-1999: Relations to source area and climate, J. Geophys. Res. Atmos., 106(D10), 10325–10333,

doi:10.1029/2000JD900665, 2001.

640   Sun, L., Li, R. B., Tian, X. P. and Wei, J.: Analysis of the temporal and spatial variation of aerosols in the Beijing-Tianjin-

Hebei region with a 1 km AOD product, Aerosol Air Qual. Res., 17(3), 923–935, doi:10.4209/aaqr.2016.05.0185, 2017.

Torres, B., Dubovik, O., Fuertes, D., Schuster, G., Eugenia Cachorro, V., Lapyonok, T., Goloub, P., Blarel, L., Barreto, A., Mallet, M., Toledano, C. and Tanré, D.: Advanced characterisation of aerosol size properties from measurements of spectral optical depth using the GRASP algorithm, Atmos. Meas. Tech., 10(10), 3743–3781, doi:10.5194/amt-10-3743-2017, 2017.

645 Tsekeri, A., Lopatin, A., Amiridis, V., Marinou, E., Igloffstein, J., Siomos, N., Solomos, S., Kokkalis, P., Engelmann, R., Baars, H., Gratsea, M., Raptis, P. I., Binietoglou, I., Mihalopoulos, N., Kalivitis, N., Kouvarakis, G., Bartsotas, N., Kallos, G., Basart, S., Schuettemeyer, D., Wandinger, U., Ansmann, A., Chaikovsky, A. P. and Dubovik, O.: GARRLiC and LIRIC: Strengths and limitations for the characterization of dust and marine particles along with their mixtures, Atmos. Meas. Tech., 10(12), 4995–5016, doi:10.5194/amt-10-4995-2017, 2017.

650 Wang, H., Xu, X. and Zhu, G.: Landscape changes and a salt production sustainable approach in the state of salt pan area decreasing on the coast of Tianjin, China, Sustain., 7(8), 10078–10097, doi:10.3390/su70810078, 2015.

Yin, Z., Ansmann, A., Baars, H., Seifert, P., Engelmann, R., Radenz, M., Jimenez, C., Herzog, A., Ohneiser, K., Hanbuch, K., Blarel, L., Goloub, P., Victori, S. and Maupin, F.: Aerosol measurements with a shipborne Sun-sky-lunar photometer and collocated multiwavelength Raman polarization lidar over the Atlantic Ocean, Atmos. Meas. Tech., 12(10), 5685–5698, 655 doi:10.5194/amt-12-5685-2019, 2019.

Yu, X., Lü, R., Liu, C., Yuan, L., Shao, Y., Zhu, B. and Lei, L.: Seasonal variation of columnar aerosol optical properties and radiative forcing over Beijing, China, Atmos. Environ., 166, 340–350, doi:10.1016/j.atmosenv.2017.07.011, 2017.

Zhai, S., Jacob, D. J., Wang, X., Shen, L., Li, K., Zhang, Y., Gui, K., Zhao, T. and Liao, H.: Fine particulate matter (PM2.5) trends in China, 2013-2018: contributions from meteorology, Atmos. Chem. Phys. Discuss., 1–19, doi:10.5194/acp-2019-660 279, 2019.

Zhu, Y., Zhang, J., Wang, J., Chen, W., Han, Y., Ye, C., Li, Y., Liu, J., Zeng, L., Wu, Y., Wang, X., Wang, W., Chen, J. and

Zhu, T.: Distribution and sources of air pollutants in the North China Plain based on on-road mobile measurements, Atmos.

Chem. Phys., 16(19), 12551–12565, doi:10.5194/acp-16-12551-2016, 2016.

Zhuang, H., Chan, C. K., Fang, M. and Wexler, A. S.: Size distributions of particulate sulfate, nitrate, and ammonium at a

665   coastal site in Hong Kong, Atmos. Environ., 33(6), 843–853, doi:10.1016/S1352-2310(98)00305-7, 1999.

670

675

680

Table 1 Instrumentation set up in the IAP mobile laboratory for the MOABAI campaign in North China Plain. The aerosol

685 **properties in italic represent the derived properties using inversion algorithms**

Instrument	Make and model	Wavelength (nm)	Temporal resolution	Aerosol physical/chemical/optical properties	Uncertainty
Micro pulse LIDAR	CE370, CIMEL	532	30 sec	Vertical profile (Attenuated backscatter) *(Extinction coefficient Mass concentration)*	15% *25% 35-45%*
PLASMA sun photometer	#650, LOA	340, 380, 440, 500, 675, 870, 940, 1020, 1640	10 sec	Column-integrated optical properties (AOD, Angstrom Exponent, precipitable water) *(Volume Size Distribution)*	2% (VIS/NIR) 3% (UV) *10-20%*
Nephelometer (3-λ)	Aurora 4000, Ecotech	450, 525, 635	30 sec	Scattering coefficient	-
Aethalometer (7-λ)	AE33, Maggee Scientific	370, 470, 520, 590, 660, 880, 950	1 sec	Absorption coefficient BC concentration	-
Optical Particle Counter (0.25-32 μm)	Sky-OPC model 1.129, GRIMM Aerosol Technik	655	6 sec	Number concentration Number size distribution PM_1, $PM_{2.5}$, PM_{10}	5%
NO-NO_2-NO_x analyser	42i, Thermo Electron	n/a	10 s	NO-NO_2-NO_x concentration	1%
SO_2 analyser	43i, Thermo Electron	n/a	10 s	SO_2 concentration	1%
O_3 analyser	49i, Thermo Electron	n/a	20 s	O_3 concentration	1%
Weather station	Airmar	n/a	1 sec	Pressure, temperature, relative humidity, wind speed/direction	-

34

Table 2 Summary of mobile transects, dates and aerosol properties observed during the MOABAI mobile measurements: AOD at 440 nm and Angstrom Exponent (AE) measured by PLASMA sun photometer and PBL height as measured by lidar

Mobile transect	Date	AOD (440 nm)	AE (440-870 nm)	PBL height, km
Beijing, 4th ring road	9 May 2017	0.62 – 0.84	0.67 – 0.87	1.7 – 2.2
Beijing, 5th ring road	11 May 2017	0.24 – 0.55	-0.03 – 0.27	1.5 – 3.6
Beijing, 5th and 6th ring road	13 May 2017	0.08 – 0.16	0.41 – 0.83	1.2 – 3.9
Beijing-Baoding-Tianjin (AB)	16 May 2017	0.2 – 0.55	1 – 1.24	0.3 – 1.7
Tianjin-Tangshan (BC)	17 May 2017	0.3 – 0.79	1 – 1.9	0.3 – 1.3
Tangshan-Beijing (CA)	18 May 2017	0.43 – 1.34	1.22 – 1.74	1 – 1.6
Beijing, 5th ring-road	19 May 2017	1.47 – 1.9	1.21 – 1.51	0.5 – 1

690 **Table 3. Mean aerosol extinction coefficients and lidar ratios (LR) at 532 nm derived from Klett AOD-constraint lidar inversions and mass concentrations in the PBL (0-2000 m), for each time interval correspondent to transect segments depicted in Fig. 4a. The standard deviations correspond to the spatio-temporal variability within each transect segment.**

Time interval	σ_{ext} (km^{-1})	LR (sr)	Mass concentration (μg m^{-3})
08:40 - 09:00	0.14 ± 0.15	66 ± 10	80 ± 85
09:00 - 09:30	0.15 ± 0.15	59 ± 17	85 ± 82
09:30 - 10:00	0.13 ± 0.10	56 ± 10	75 ± 57
10:00 - 10:30	0.14 ± 0.07	52 ± 12	80 ± 41
10:30 - 11:00	0.13 ± 0.06	50 ± 11	74 ± 34
11:00 - 11:30	0.14 ± 0.06	43 ± 14	78 ± 33
11:30 - 12:00	0.1 ± 0.06	46 ± 14	57 ± 34
12:00 - 12:30	0.18 ± 0.09	40 ± 13	100 ± 50
12:30 - 13:00	0.16 ± 0.13	35 ± 12	88 ± 72
13:00 - 13:30	0.15 ± 0.13	39 ± 11	83 ± 71
13:30 - 14:00	0.15 ± 0.13	45 ± 11	87 ± 74
14:00 - 14:30	0.13 ± 0.11	42 ± 8	73 ± 60
14:30 - 15:00	0.13 ± 0.12	52 ± 12	71 ± 65
15:00 - 15:30	0.13 ± 0.12	47 ± 11	75 ± 66
15:30 - 16:00	0.13 ± 0.11	57 ± 14	71 ± 59

Atmospheric
Chemistry
and Physics
Discussions

Table 4. Parameters used for the calculations of mass concentration: modal radius for fine, r_{mf}, and coarse, r_{mc}, mode, in μm, the geometric standard deviation for fine, σ_f, and coarse, σ_c, mode, the ratio of volume concentration of coarse to fine mode, C_c/C_f,

695 **the particle density, ρ, in g cm^{-3}, the real part of the refractive index, m_r and the imaginary part of the refractive index, m_i.**

	r_{mf}	r_{mc}	σ_f	σ_c	C_c/C_f	ρ	m_r	m_i
mean	0.13	1.66	0.43	0.68	0.8	1.75	1.5	0.01
std	0.01	0.03	0.01	0.03	0.1	0.34	0.05	0.005
impact on mass (PBL)	7 %	0.5 %	0.7 %	0.6 %	4 %	20 %	13 %	1 %
impact on mass (dust)	-	2 %	-	3 %	-	20 %	1 %	0.1 %

700
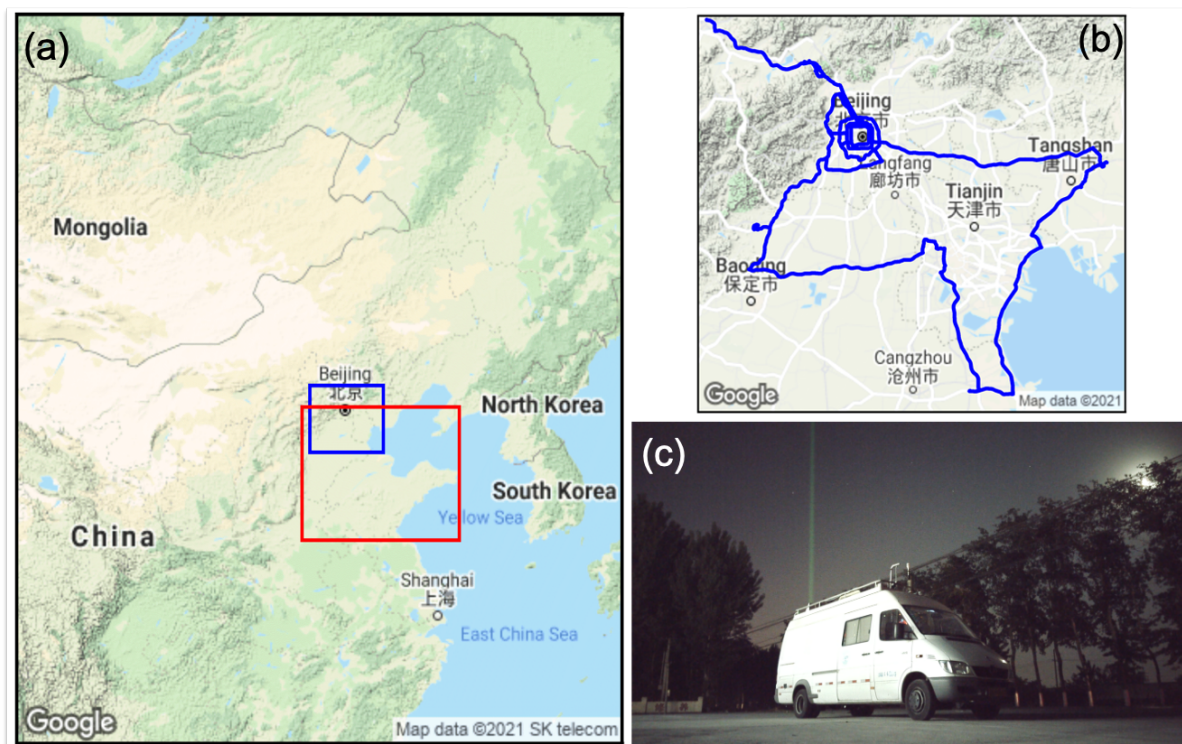
Figure 1: (a) Map of China and neighbour regions showing North China Plain (red rectangle) and area investigated through mobile measurements (blue rectangle), (b) GPS track of all mobile transects and (c) IAP's instrumented van used for the mobile observations; photograph taken at night on 17 May 2017 at Guye (39.71° N, 118.37° E), near Tangshan.
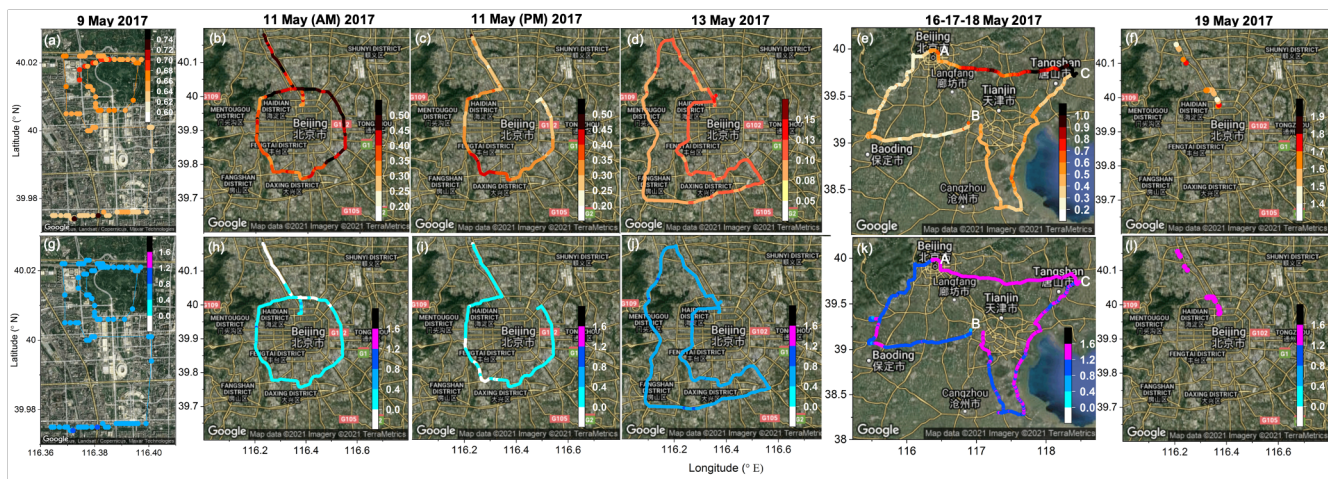
Figure 2. Spatial variability of AOD at 440 nm and (top panels) and Angstrom Exponent (AE) between 440 and 870 nm (bottom panels), derived from PLASMA sun photometer measurements. The A, B and C (Fig. 2d and 2k) denote the departure and end points for the three transects: Beijing-Tianjin (AB) on 16 May 2017, Tianjin-Tangshan (BC) on 17 May 2017 and Tangshan-Beijing (CA) on 18 May 2017. Please note that the color scale for the AOD maps is different for each transect in order to show the fine spatial variability.
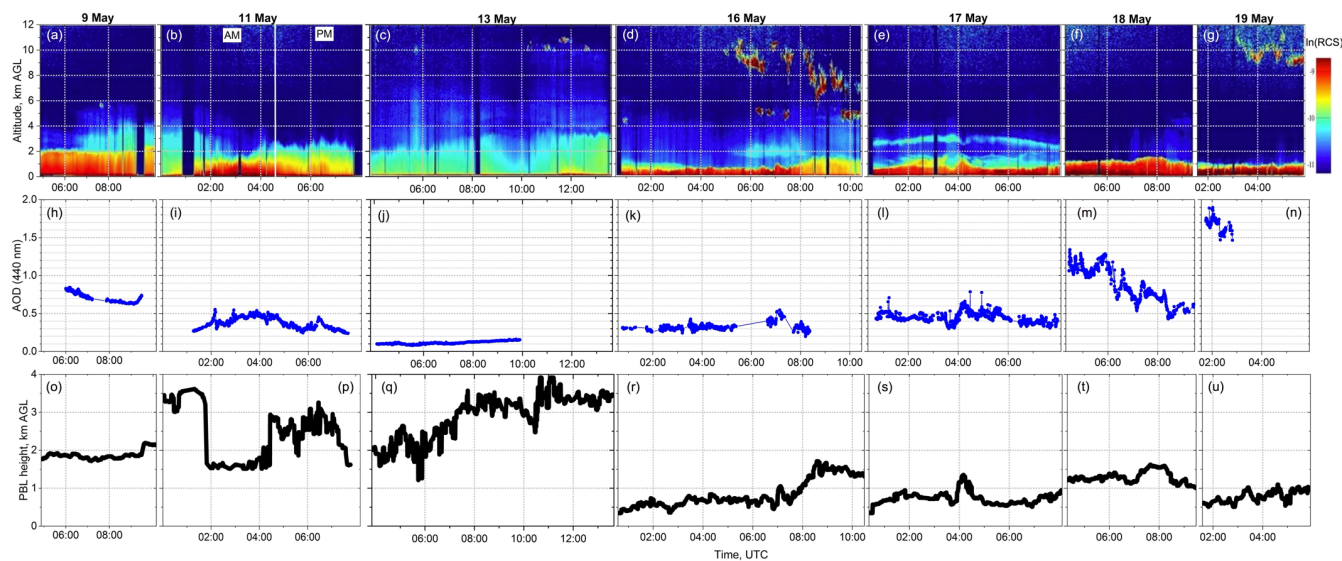
Figure 3. (Top panels) Spatio-temporal and vertical variability of aerosol layers and clouds, colour-coded by lidar Range Corrected Signal (RCS) as measured along the mobile transects detailed in Table 2, (Middle panels) AOD at 440 nm and (Bottom panels) PBL height.
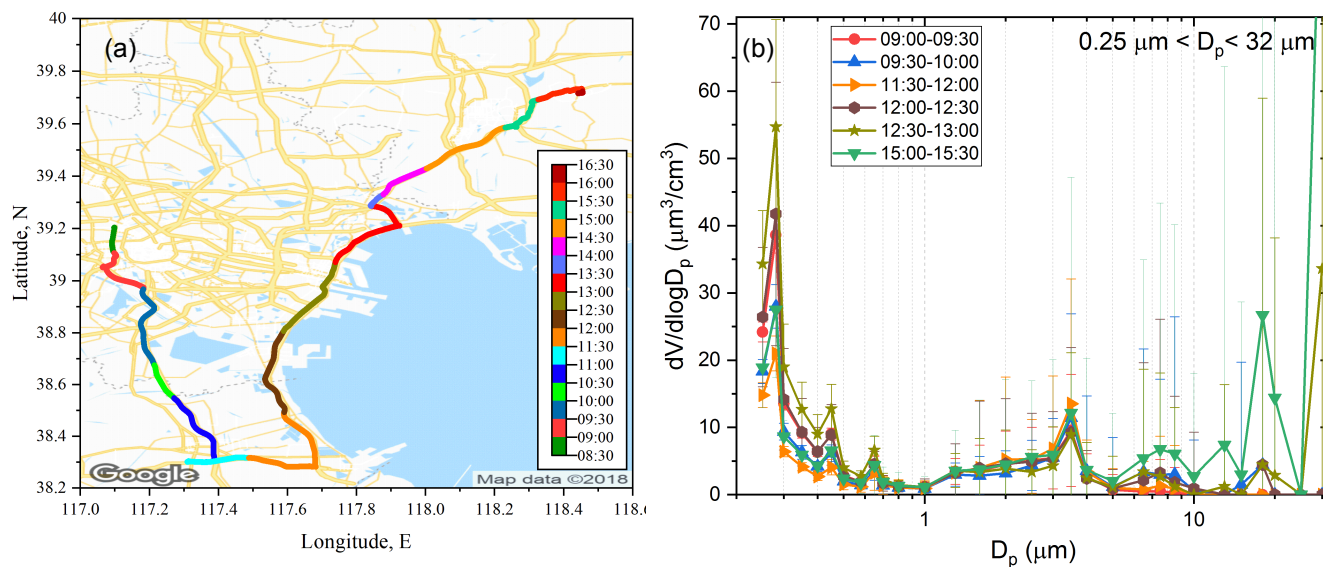
Figure 4. (a) GPS track of the mobile transect from Tianjin to Tangshan color coded by 30 minutes time intervals (local time, UTC+8 h) and (b) particle volume size distributions measured by Grimm Sky-OPC, averaged on 30 minutes transect segments.
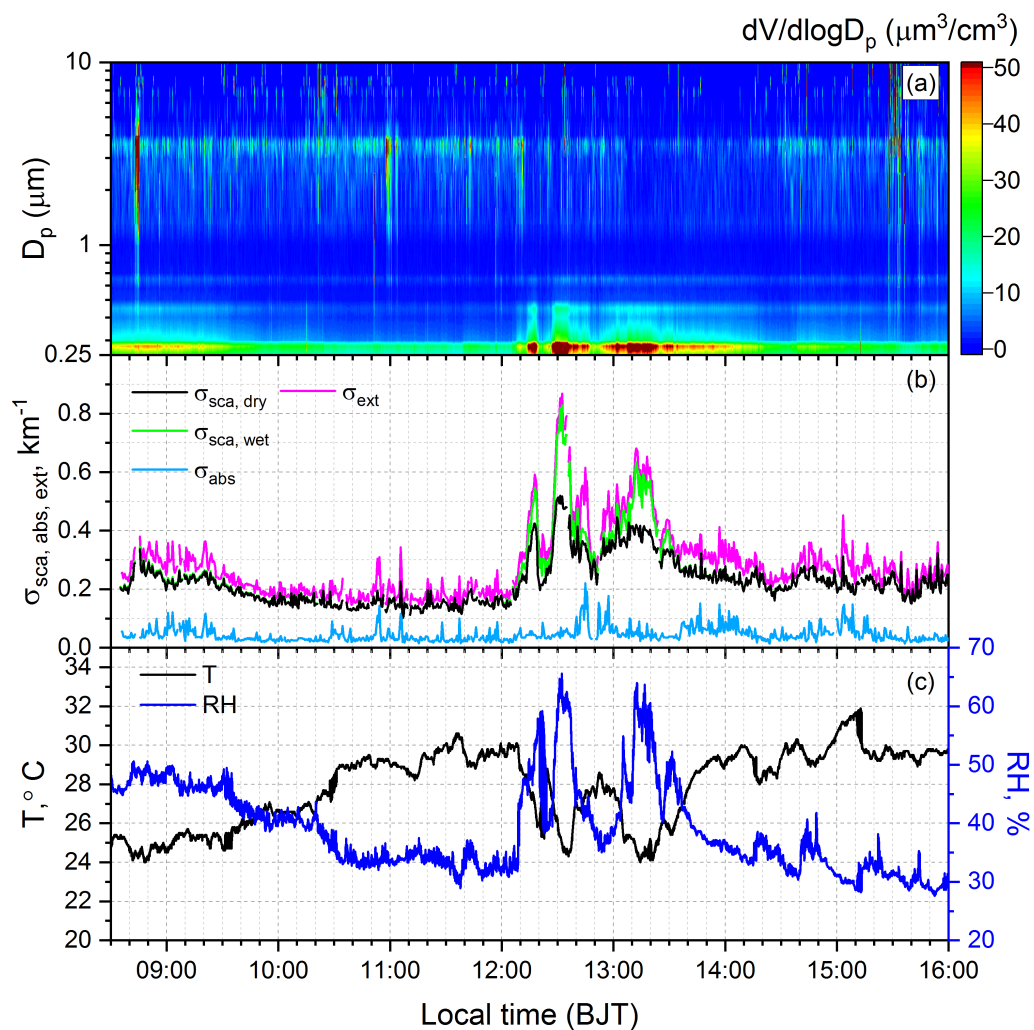
Figure 5. Spatio-temporal variability of (a) particle volume size distribution as measured by Grimm Sky-OPC, (b) scattering coefficient measured by nephelometer (black), scattering coefficient corrected for relative humidity effect (green), absorption

725 **coefficient derived from aethalometer measurements (light blue), extinction coefficient computed from nephelometer and aethalometer measurements (magenta) and (c) temperature (T) (black) and relative humidity (RH) (blue) measured by the weather station along the mobile transect from Tianjin to Tangshan on 17 May 2017.**

Atmospheric
Chemistry
and Physics
Discussions
Open Access
EGU
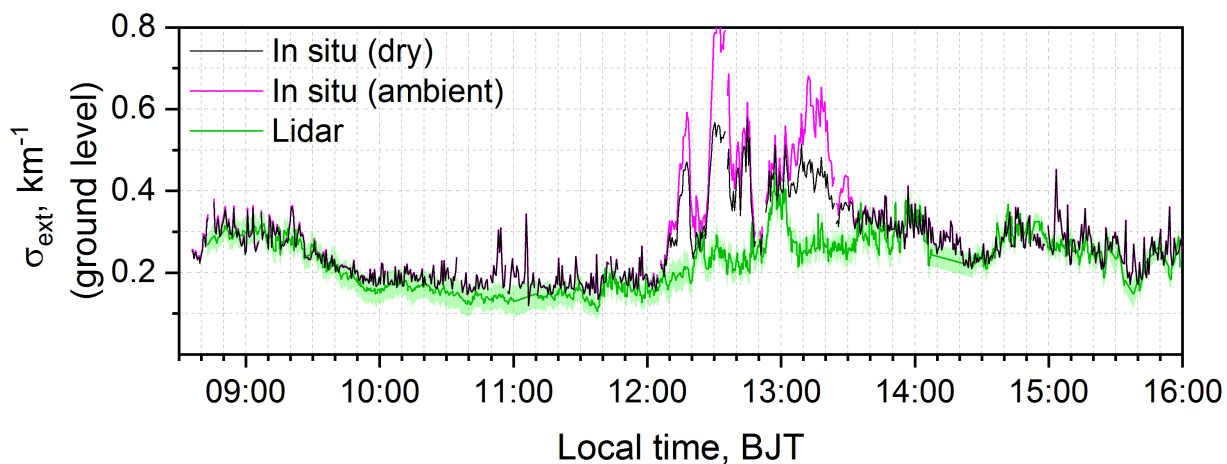
Figure 6. Spatio-temporal variability of aerosol extinction coefficient at 525 nm derived from in situ measurements (nephelometer and aethalometer) with no correction for RH (black) and with $f(RH)$ correction (magenta) and lidar-derived extinction coefficients at 532 nm at 210 m altitude (green). The green shaded area represents the uncertainty on the derived extinction coefficient.
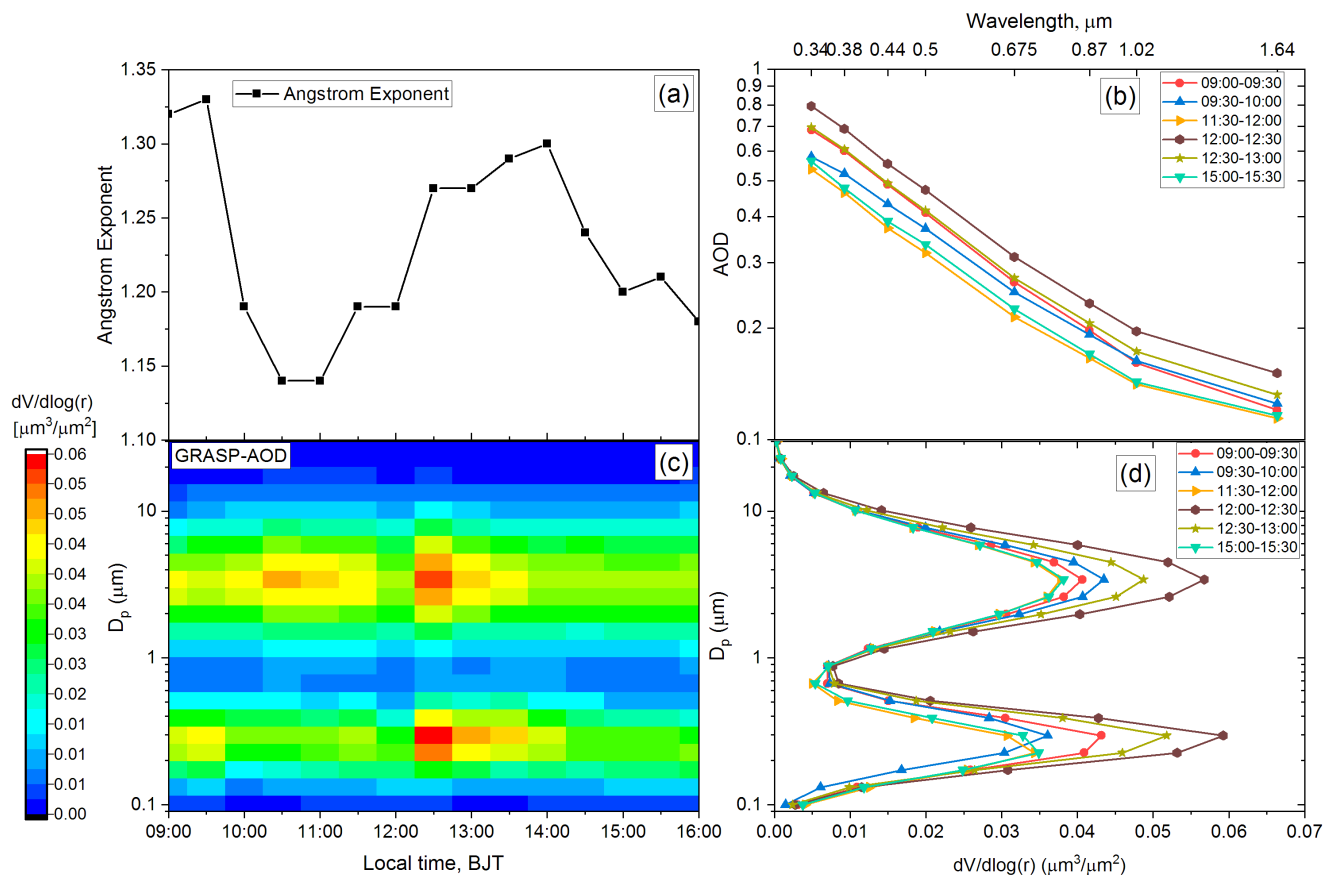
Figure 7. Spatio-temporal variability of (a) Angstrom Exponent (AE), (b) spectral AOD, (c) total column volume size distributions retrieved with GRASP-AOD for every transect segment and (d) columnar volume size distributions for some time intervals along the mobile transect. All size distributions are averaged on 30 minutes time intervals and can be localized on the mobile transect using the map color coded by local time shown in Fig. 4a.
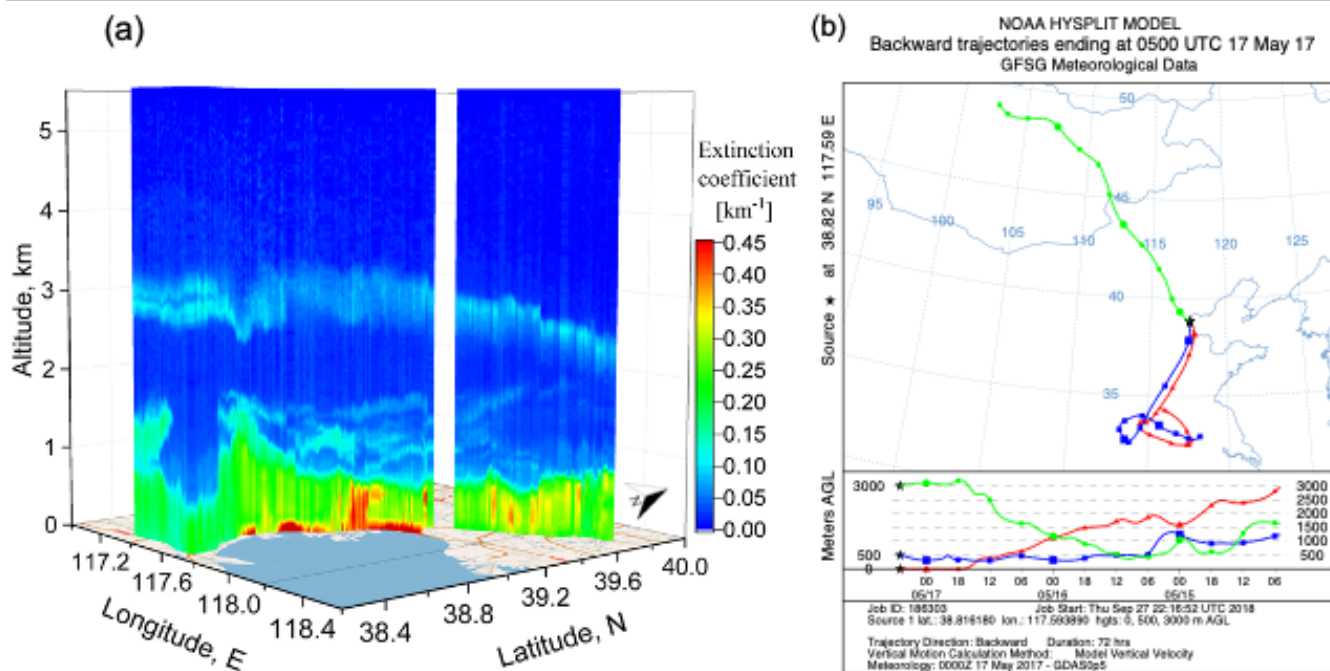
740 **Figure 8. (a) 3-D representation of the lidar-derived extinction coefficients profiles at 532 nm along the mobile transect from Tianjin to Tangshan and (b) 72 h backward trajectories (Stein et al., 2015 ; HYSPLIT, 2018) arriving at a point along the mobile transect, near Tianjin port (38.82° N, 117.59° E) on 17 May 2017, 05:00 UTC at heights of 0 m (red), 500 m (blue) and 3000 m (green) above ground level.**
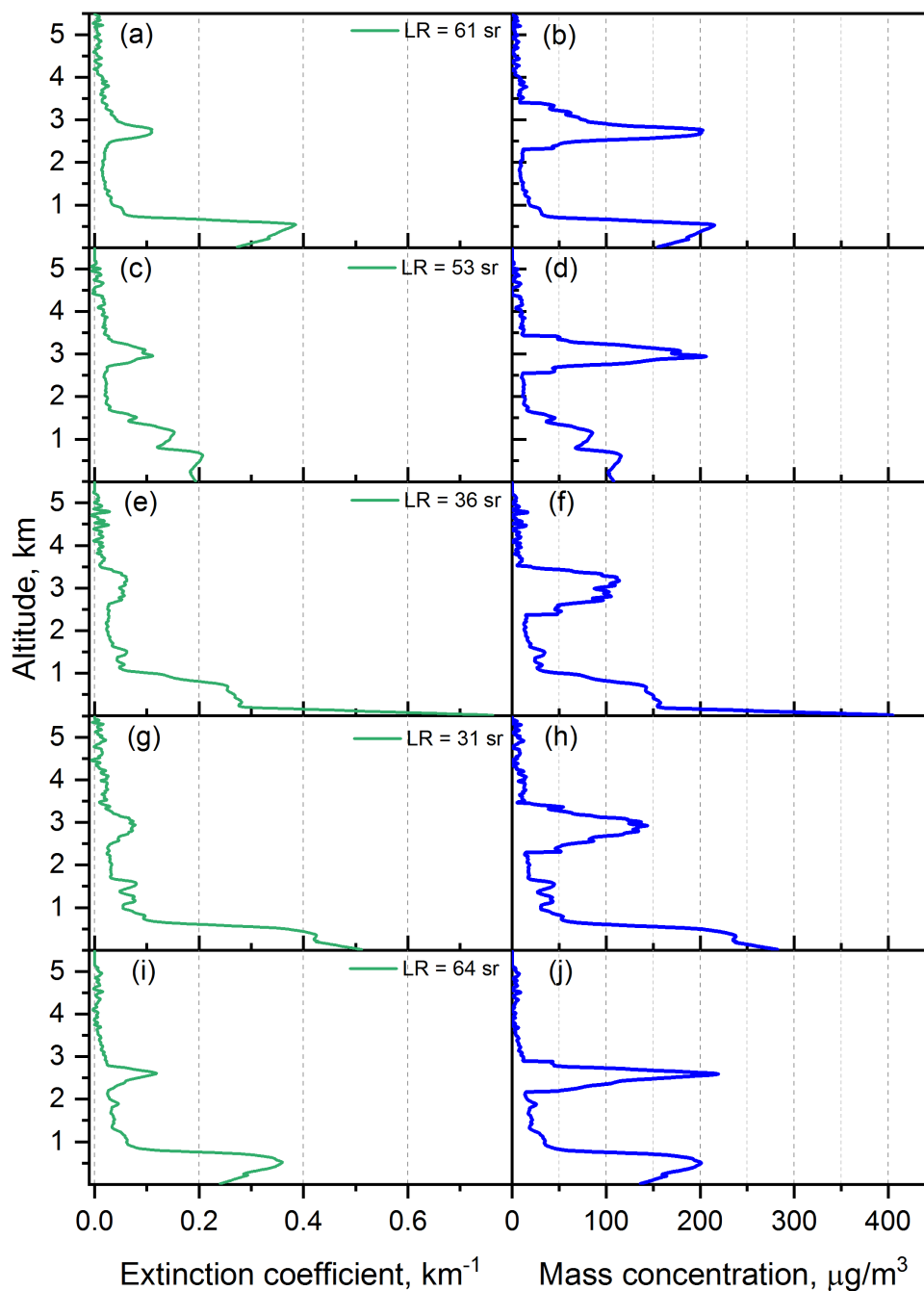
Figure 9. (Left) Aerosol extinction coefficient profiles and lidar ratios at 532 nm and (Right) total mass concentrations profiles for different times along the mobile transect: 08:55 (a, b), 10:50 (c, d), 12:30 (e, f), 13:00 (g, h) and 15:20 (i, j), local time. The extinction profiles were derived using the in situ constraint corrected for RH.

745
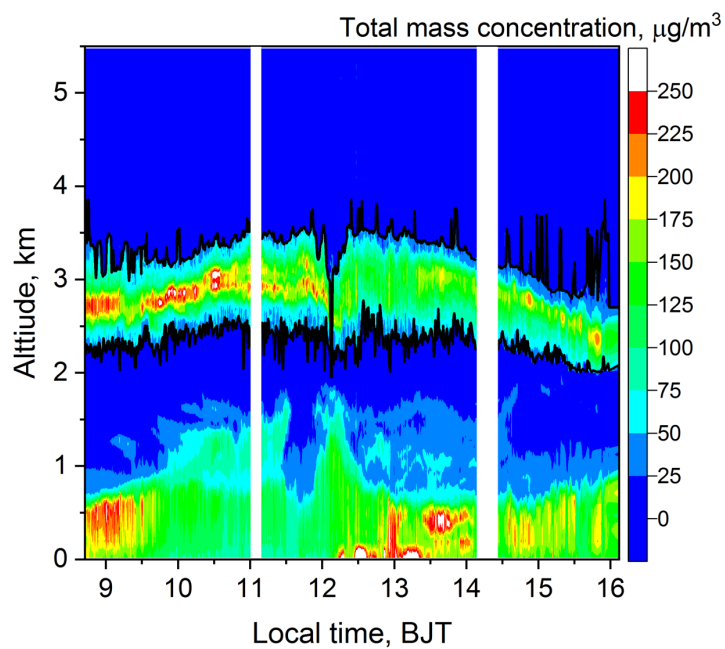
Figure 10. Aerosols total mass concentration profiles derived using the MEE approach on 17 May 2017 along the transect from Tianjin to Tangshan (BJT=Beijing time). The calculations were done considering a dust aerosol model for the layer in the 2000-3500 m range and an urban-industrial aerosol model for the rest of the profile.
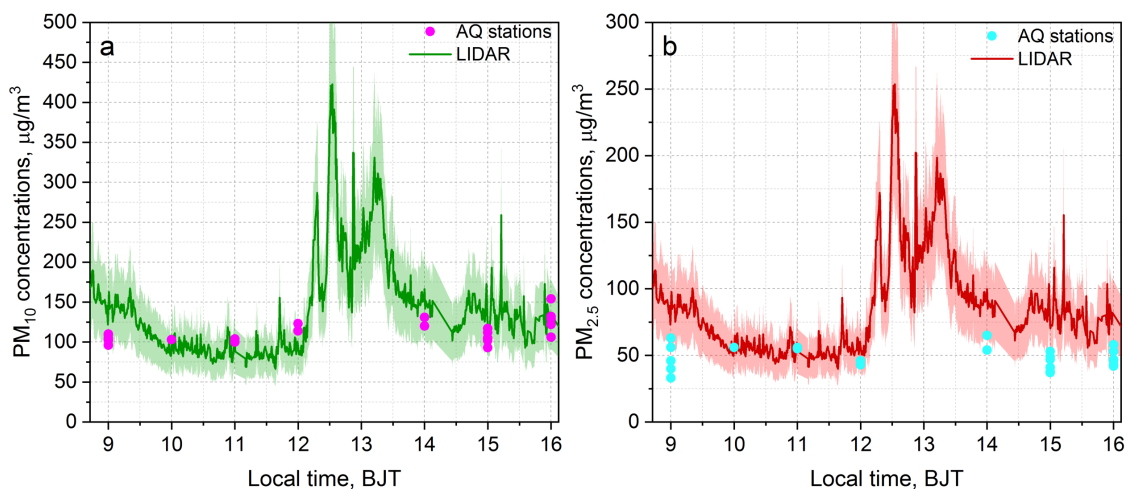
Figure 11. Spatio-temporal variability of (a) PM$_{10}$ (green) and (b) PM$_{2.5}$ (red) at surface level derived from lidar profiles and the mean hourly PM$_{10}$ (magenta) and PM$_{2.5}$ (cyan) measured at the closest air quality (AQ) stations to the route (BJT=Beijing time). The shaded area on each curve represents the uncertainty of 32% on the lidar-derived mass concentrations.